Icarus 432 (2025) 116465

Contents lists available at ScienceDirect

Icarus

journal homepage: www.elsevier.com/locate/icarus

Research Paper

# Multi-instrument sounding of a Jovian thunderstorm from Juno

Shawn R. Brueshaber [a,*], Zhimeng Zhang [b], John H. Rogers [c], Gerald Eichstädt [d], Glenn S. Orton [e], Davide Grassi [f], Leigh N. Fletcher [g], Cheng Li [h], Shinji Mizumoto [i], Alessandro Mura [f], Fabiano Oyafuso [e], Ramanakumar Sankar [j], Michael H. Wong [j,k], Candice J. Hansen [l], Steven Levin [e], Scott Bolton [m]

[a] Mechanical and Aerospace Engineering Department, Michigan Technological University, 1440 Townsend Dr., Office: R.L Smith Bldg. Office 824, Houghton, MI, 49931, United States of America
[b] Division of Geological and Planetary Sciences, California Institute of Technology, Pasadena, CA, United States of America
[c] British Astronomical Association, London, United Kingdom
[d] Independent Scholar, Stuttgart, BW, Germany
[e] Jet Propulsion Laboratory/California Institute of Technology. Pasadena, CA, United States of America
[f] Institute for Space Astrophysics and Planetology INAF-IAPS, Roma, RM, Italy
[g] School of Physics and Astronomy, University of Leicester, Leicester, United Kingdom
[h] Department of Climate and Space Sciences and Engineering, University of Michigan, Ann Arbor, MI, United States of America
[i] Association of Lunar and Planetary Observers (ALPO)., Japan
[j] Center for Integrative Planetary Sciences, University of California, Berkeley, CA, United States of America
[k] Carl Sagan Center for Research, SETI Institute, Mountain View, CA, United States of America
[l] Planetary Science Institute, Tucson, AZ, United States of America
[m] Space Science and Engineering Division, Southwest Research Institute, San Antonio, TX, United States of America

## ARTICLE INFO

Dataset link: https://pds-atmospheres.nmsu.edu/data_and_services/atmospheres_data/JUNO/microwave.html, https://pds-atmospheres.nmsu.edu/PDS/data/jnomwr_1100/data_calibrated/, https://pds-imaging.jpl.nasa.gov/volumes/juno.html, https://atmos.nmsu.edu/PDS/data/PDS4/juno_jiram_bundle/data_calibrated/, https://alpo-j.sakura.ne.jp/Latest/j_Cylindrical_Maps/j_Cylindrical_Maps.htm

*Keywords:*
Jupiter (873)
Atmospheric dynamics (2300)
Radio astronomy (1338)
Atmospheric composition (2120)
Atmospheric structure (2309)

## ABSTRACT

Thunderstorms play a significant role in transporting heat from the deep interior to space on giant planets. We present observations of a 3,400-km wide thunderstorm complex in Jupiter's North Equatorial Belt (NEB) during the 38th periapse of the Juno spacecraft on 29 Nov. 2021. Data were acquired by the Microwave Radiometer (MWR), the visible light JunoCam instrument, the Jovian InfraRed Auroral Mapper (JIRAM), and from supporting Earth-based imaging. This was the first time Juno was able to observe a thunderstorm at suitably low emission angles with multiple instruments at close range (~5,690 km), making it the most comprehensive close-up assessment of a Jovian thunderstorm to date. Lightning detection confirmed the Storm's vigorous convective nature. MWR brightness temperatures indicate this Storm appears to be wholly contained within the weather layer, i.e., no deeper than the expected base of the $H_2O$ cloud, and not as a result of any detected deep-seated upwelling beneath the $H_2O$ cloud base. Earth-based observations tracked it over its ~ 2-week lifespan, providing evidence that mesoscale-to-synoptic-scale forcing mechanisms were involved in sustaining it, including the intriguing possibility of a humidity front ('dryline'), a sharp gradient in the vapor abundance, promoting lift along a concentrated region.

## 1. Introduction

The Juno spacecraft passed nearly overhead of a 3,430-km wide thunderstorm complex, hereafter the *'PJ38 Storm', or 'Storm'*, centered at 8°N (planetocentric, 'PC'), 89°W longitude (System III) in the North Equatorial Belt (NEB) during its 38th periapse ('perijove'; 'PJ') on 29 Nov. 2021. This overpass enabled observations of a Jovian thunderstorm with the Microwave Radiometer (MWR) (Janssen et al., 2017; Oyafuso et al., 2020), and JunoCam (Hansen et al., 2017) instruments at close range (~5,690 km). The Jovian Infrared Auroral Mapper (JIRAM) (Adriani et al., 2017) also captured the Storm several hours prior to periapse. The MWR probes the atmosphere from a pressure of ~ 700 mbar to hundreds of bars, and captured numerous lightning flashes confirming the Storm's vigorous moist convective nature. MWR data also show no compositional or thermal anomalies deeper than the base of the $H_2O$ cloud, unlike some discrete vortices (Bolton et al., 2021) and belts/zones, which show microwave brightness temperature

* Corresponding author.
*E-mail address:* srbruesh@mtu.edu (S.R. Brueshaber).

https://doi.org/10.1016/j.icarus.2025.116465
Received 31 July 2024; Received in revised form 30 December 2024; Accepted 22 January 2025
Available online 10 February 2025

inversions below the expected base of the $H_2O$ clouds. Rather than a deep origin for this Storm, we find that a dryline (i.e., a 'humidity front'; (Markowski and Richardson, 2010)) within the weather layer may explain both the long duration of this Storm and the lack of a brightness temperature inversion detected in the microwave. A dryline is a narrow discontinuity in air density as a result of vapor abundance, analogous to the density discontinuity that occurs across a temperature front. In this paper, we follow previous convention to define the weather layer as the base of the $H_2O$ cloud layer to the tropopause (e.g., Fletcher et al., 2020).

The NEB typically appears as a wide dark belt with turbulent cloud features and convective outbreaks, the latter appearing as white spots that quickly distort into white filaments. The NEB(s) contains dark festoons often associated with bright plumes around 7–8°N PG latitude, which have long been known from ground-based observations (Rogers, 1995) and closely studied by spacecraft (Fountain et al., 1974), (Stoker, 1986) (Stoker and Hord, 1985) (Vasavada et al., 1998), (Choi et al., 2013), and reviewed more recently (Rogers, 2019a). However, this normal aspect ceased in 2021, setting the stage for a different type of transient convective storm as described in this paper.

### 1.1. The north equatorial belt in 2021

The most continuous record of changes of Jupiter's visible cloud deck comes from a near-nightly series of amateur observations of Jupiter, which provide valuable context to our Storm analysis. Early in 2020, the NEB(n), covering ~12–15°N, exhibited wave-like undulations, followed by a whitening of its typical dark color, leaving only a very narrow dark NEB(s) (7–11°N) with a pale NEB(n) by mid 2021 ("Fading") (Rogers, 2021a,b; Rogers et al., 2022). This state of the NEB resembles one just prior to a re-darkening ("Revival") of a similarly atypical bright NEB in 2012. Such vigorous revivals that dramatically return the NEB to its broad dark rust-colored appearance are rare, the last event prior to 2012 — which occurred during solar conjunction — was in 1926 (Rogers, 2019a,b; Rogers and Adamoli, 2019c). Less extreme expansions of the NEB northwards are more common, with a 3–5 year period observed in the visible and infrared, and typically begin with outbreaks of bright white spots with rapidly changing morphology, strongly suggestive of vigorous moist convection (Rogers, 2019a, 2021a). As these white convective upwellings are compensated by subsidence, warming and aerosol clearing occurs, returning the belt to its typical state. An analogous process has been observed for an SEB Revival in 2010–2011 (Fletcher et al., 2017). It too started with discrete storm outbreaks at a particularly active longitude. A deeper understanding of the dynamics was not available from Earth. However, this NEB Storm outbreak, described in this paper, was witnessed from Juno including the novel observations provided by the MWR instrument.

By early 2021, deep moist convective activity had ceased in the NEB. However, even as the belt continued to whiten and the usual large dark formations on its south edge disappeared, small short-lived convective eruptions resumed at ~10°N (PC): two of them in May 2021, and more from August 2021 onwards, all at a single active longitude drifting eastward at ~7.0°/day to 5.7°/day (Sys. III) (Rogers et al., 2022; Rogers, 2021c, 2022; Wong et al., 2023). Such episodic small storms also occur during a typical NEB state, but in 2021 they were the only manifestation of renewed convective activity in the NEB. All these storms drifted south while accelerating eastward.

### 1.2. Physics of drylines and thunderstorms

The NEB(s) straddles a transition between the $NH_3$-enriched Equatorial Zone (EZ) and the $NH_3$-depleted NEB (Li et al., 2017). This gradient in $NH_3$ abundance is the largest known on the planet and is a persistent feature as Juno's 8 years in orbit at the time of this writing has revealed. Gradients in $H_2O$ vapor abundances (humidity) on Earth are often associated with mesoscale convective complexes (MCC; (Maddox, 1980)). MCCs are composed of multiple thunderstorm cells that are in various stages of their lifecycles, i.e., formation, maturation, and dissipation. MCCs are often found, among other places, in the Great Plains of North America and the Sahel region of Africa during the summer. Development of these MCCs is often triggered by lift from a cold front. However, they are also sometimes created by the advection of moist and dry airmasses of nearly identical temperature along a narrow humidity gradient, known as a 'dryline.' Such drylines operate similar to a cold front in that one side contains air of greater density moving under and lifting air of less density on the other side.

Drylines are favorable for thunderstorm formation, including those in MCCs (Markowski and Richardson, 2010; Bluestein and Parker, 1993). Eddy transport of moist air from Jupiter's EZ into the drier NEB(s) may favor the formation of a dryline, similar to the advection of dry continental air into and under moist tropical airmasses on Earth. On Jupiter, however, an $H_2O$-rich air mass originating in the EZ may be stable to convection because its greater molecular weight can support an otherwise unstable superadiabatic lapse rate (Cheng et al., 2024). This would tend to displace the more buoyant drier air upwards, opposite of the situation on Earth. However, mixing of these airmasses along the dryline through small-scale turbulence and parcel motion may be enough to reduce the molecular weight suppressing effect making the superadiabatic lapse rate unstable to convection. On Earth, such mixing occurs via entrainment along the sides of cumulus clouds, along a front or dryline, or at the top of the planetary boundary layer. Moistening of a dry layer that suppresses convection (i.e., a 'cap') is a common occurrence that often leads to thunderstorm formation. Once the cap is eroded by this moistening, a lucky cumulus cell, aided by previous cells depositing moisture into the cap and weakening its convective suppressing effect, punches upward through the cap leading to thunderstorm development. Recent primitive-equation model (Vallis, 1996) simulations by Sankar et al. (2024) for Jupiter find that eddy transport of water is an effective mechanism to increase convective potential energy, generate convective instabilities, and support drylines as a formation and maintenance mechanism. If $H_2O$ abundance distribution in the NEB and EZ is also subjected to a similarly strong gradient as $NH_3$ is, then we may have a region that is climatologically favorable to thunderstorm formation, which matches the observations of the stormy NEB dating back to the Pioneer and Voyager epochs.

The NEB's cyclonic environment is also favorable for the development of thunderstorms. Several authors such as Dowling and Gierasch (1989), Thomson and McIntyre (2016), Fletcher et al. (2017), Fletcher et al. (2020) have postulated that the air in the cyclonic belts feature a relatively short vertical distance from the $H_2O$ lifting condensation level (LCL) to the level of free convection (LFC). This concept is supported by the isentropic potential vorticity perspective (IPV) of cyclonic regions (Hoskins et al., 1985; Allison, 2000), which states that isentropes bulge upward in the lower part of the weather layer. Air flows along these isentropes and, as it ascends, it adiabatically cools.

A layer of air, which may be initially stable against vertical parcel motion, flows upward along these isentropes as a result of advection. If the bottom portion contains more moisture than the top, the bottom condenses clouds before the top does. As the layer of air continues to rise, the bottom cools at the slower moist adiabatic rate than the top, which continues to cool at the faster dry adiabatic rate. The overall effect is that any previously stable lapse rate in this layer of air may become conditionally unstable; i.e., the ambient lapse rate is between a dry and a moist adiabat. On Earth, this is a well-known phenomena and is termed 'potential instability' (Holton, 2004). Conditionally unstable air is one that is unstable if cloud condensation occurs, but is stable if no cloud condensation occurs (see e.g., (Holton, 2004), (Houze, 2014)).

Any additional mesoscale forcing promoting lift and condensation, such as from a dryline, could more easily set off a convective outburst. Subsequent vertical parcel motion in this now conditionally unstable layer may allow cells to adiabatically cool sufficiently for cloud condensation to occur. Once condensation occurs, the parcel is convectively

unstable (it is at its LFC), and will erupt upwards releasing convective available potential energy (CAPE). It could very well be that potential instability, a short vertical distance from the LCL to the LFC, and the removal of the stabilizing effect of a molecular weight gradient effect through mixing with drier air all contribute to thunderstorm development in the NEB(s).

## 2. Observations

### 2.1. Earth-based observations

The PJ38 Storm observed from Juno instruments on Nov. 29, 2021, had a complex evolution from ground-based observations. The Storm formed on or about Nov. 18, which we reference as Day 1 (Rogers, 2021c) in the EZ-NEB(s) transition region near the limb at 120 ° System I longitude (Fig. 1a). This was the sixth convective eruption at an active drifting longitude in 2021. Fig. 1 details the evolution of the PJ38 Storm observed by skilled amateur astronomers using RGB, UV and IR (e.g., 889 nm) filters, and by images acquired from NASA's Infrared Telescope Facility at 5.1 μm. See Supplemental Materials Fig. S1 showing a larger longitudinal span of these images.

Day 4 provides the first clear image of the Storm (Fig. 1b) surrounded by the rust-colored clouds of the NEB(s), but not yet in contact with the ochre-colored clouds of the Equatorial Zone (EZ). The first two 889-nm $CH_4$ images (Fig. 1c & Fig. 1g on Days 4 & 6, respectively) reveal a bright Storm, indicative of vigorous convective upwelling, injecting material high into the troposphere. To the east, starting on Day 4 (Figs. 1b and 1c) and persisting through Day 13, is a patch that is dark at 889 nm, and dark blue-gray in color composite, typical of cloud-clearing within 5-μm hotspots, and in segments within belts. On Day 5, the Storm's bright center 'core' featured a 'tail' extending to the west-northwest (Fig. 1d), likely caused by the prevailing horizontal wind shear. By Day 9 (Fig. 1i and 1i'), three days prior to perijove, the Storm appears to have contacted the clouds of the EZ and the formerly elliptical core dramatically changed appearance. A small region of bright reddish-hued clouds appears to the east-southeast of the bright Storm core with a translucent cirrus cloud shield evident to the west, which appears as marked by the arrow in Panel i'. Fig. 1j (Day 10), while blurry, shows the Storm's clouds expanding along the boundary with the EZ. Fig. 1k (Day 10), a 5-μm image, shows a dark 'notch' at the location of the RGB-bright Storm clouds extending east and south to the EZ. A festoon-like feature (arrows in Panel k') is also faintly visible, extending SW from the NEB(s) and passing south of the core. On Day 11, the 889-nm filter (Fig. 1l) shows that the core appeared to merge with a modestly bright SW-NE oriented EZ plume feature. The RGB image on Nov. 30 (Fig. 1n; Day 13) reveals that the Storm's morphology dramatically changed again, flattening out along the EZ. On Days 13–16, the Storm appears to have largely merged with the EZ, and, after Day 16 (Fig. 1o), it is no longer identifiable. Presumably its store of moisture was exhausted, its lifting mechanism was cut off, or the atmosphere became stable against convection once again.

Eruptions of convective activity along a common drifting longitude suggest an underlying disturbance as a driving mechanism for the series of individual convective eruptions collectively termed *stealth superstorms* (Wong et al., 2023) (Wong et al., 2004). The term 'stealth' was coined because the storm spots were *'not extremely bright in methane filter bands, and because they were episodic rather than continuously active over the 2021–2022 period.'* (Wong et al., 2023). The nature of this underlying disturbance that episodically generated these storms is not entirely clear. All of these eruptions, including the PJ38 Storm (Fig. 2a, b), appeared around ~9°N (PC), and drifted westward in Sys. I, which moves at System III-7.364°/day (Fig. 2d). These storms drifted southward then re-curved eastward being caught in the prograde jet, typically located at ~ 6–7°N (Rogers, 2021c), shown in Fig. 2c. It should be recognized, though, that these zonal wind profiles are snapshots in time. The Asay-Davis et al. profile (Asay-Davis et al., 2011) shows a peak at 8°N rather than at 6–7°N and probably represents the best fit from amateur measurements for equatorial features (south of the Storm) observed in 2021. Interestingly, Juno flew near another thunderstorm outbreak during PJ39 (spot 8 in Fig. 2d). By this time, the underlying disturbance that was spawning these storms in 2021 was expanding in longitude, a behavior previously witnessed in the SEB in 2010–2011 (Fletcher et al., 2017). Unfortunately, the ground track was far enough away that the MWR instrument's footprints did not capture it.

Fig. 2d shows a plot of the storm activity in the NEB(s) from early August 2021 into February 2022. The PJ38 Storm is towards the center of the panel. The small dark open circle markers represent a very bright compact spot ('Eruption'). The small red circle markers represent a more weakly bright or less well-defined spot, or one moving southward ('Sign/Shift-S/Weakening'). The dark filled small circle markers represent a pronounced dark spot in methane filtered images ('CH4-dark patch'), possibly the result of cloud clearing in the wake of a storm. Small blue–green circles represent short duration spots noted by the amateur community.

The locus of origin of the storms, including Spots 1 and 2 (not shown here), fitted a range of drifts from +0.4 to +1.7 °/day in Sys. I (Rogers, 2021c), suggesting that the superstorm had variable drift and/or was becoming longitudinally extended during the year. Spots 3, 4, 5, 7, and 8 appeared to start along a common drifting origin with a drift rate of ~0.4°/day in Sys. I. Spot 6 (the PJ38 Storm) and spot 9 appeared a bit west of this drift line but otherwise behaved much the same as the previous spots in the NEB(s) during this unusual state of the NEB and probably are the result of the same disturbance beginning to broaden its influence because after the end of 2021, the activity increased in the NEB(s) with multiple outbreaks at different longitudes occurring throughout 2022. As of late 2023 and 2024, the NEB has returned to its usual wide, dark-banded appearance.

### 2.2. JunoCam observations

JunoCam captured the PJ38 Storm morphology in great detail on Nov. 29, 2021 (Day 12), with its closest approach to the storm's 1-bar level at 5,690 km, as shown in Fig. 3a & b. In these figures, the RGB colors have been stretched to improve contrast and re-projected to a resolution of 3 km/pixel, which is not much smaller than the original 3.8 km/pixel in the neighborhood of the Storm's core. The ~3,430-km wide Storm system is characterized by an optically thick bright core (Fig. 3a item 4, Fig. 3b item 4b), with a thick anvil cloud overtop the core's cumulonimbus (thunderstorm) towers. A thin, large, translucent, and cirrus cloud shield is located mostly to the west and south of the core (Fig. 3a items 1 & 2). This shield also shows some morphological changes from the Nov. 26 map (Fig. 1i), suggesting temporal variations in convective activity. The areal extent of the Storm complex, which includes items 1–4 is $5.6 \times 10^6$ km$^2$, with the bright core (Fig. 3a item 4, Fig. 3b item 4b) covering $1.0 \times 10^6$ km$^2$ (see Methods Section 4.2). The curvature of small cirrus filaments (arrows) near the core suggest possible anticyclonic circulation at the cloud top (dashed lines), consistent with diverging outflow at the stable upper troposphere being rotated by the Coriolis force. Immediately east of the Storm core, bright clouds appear orange due to a thin red–orange haze (Fig. 3a, item 3) that appears to be overtop what otherwise would likely be bright white clouds. Fig. 3b shows a close-up of the Storm core as denoted by the oval (Fig. 3b, item 4b). Here, we observe the brightest clouds in the storm complex although there are slightly dimmer, faintly bluish patches visible from the center of the oval NW along the major axis. Given the direction towards the Sun (yellow arrow), these may be shadowing effects from overshooting convective tops just to the east, or more likely, regions of the core with decaying cells. Interestingly, along the minor axis of the oval marker on the east side, a distinctly red–orange patch appears thicker to the east of the core. These cells may be at the same altitude as the core but appear lower due to the

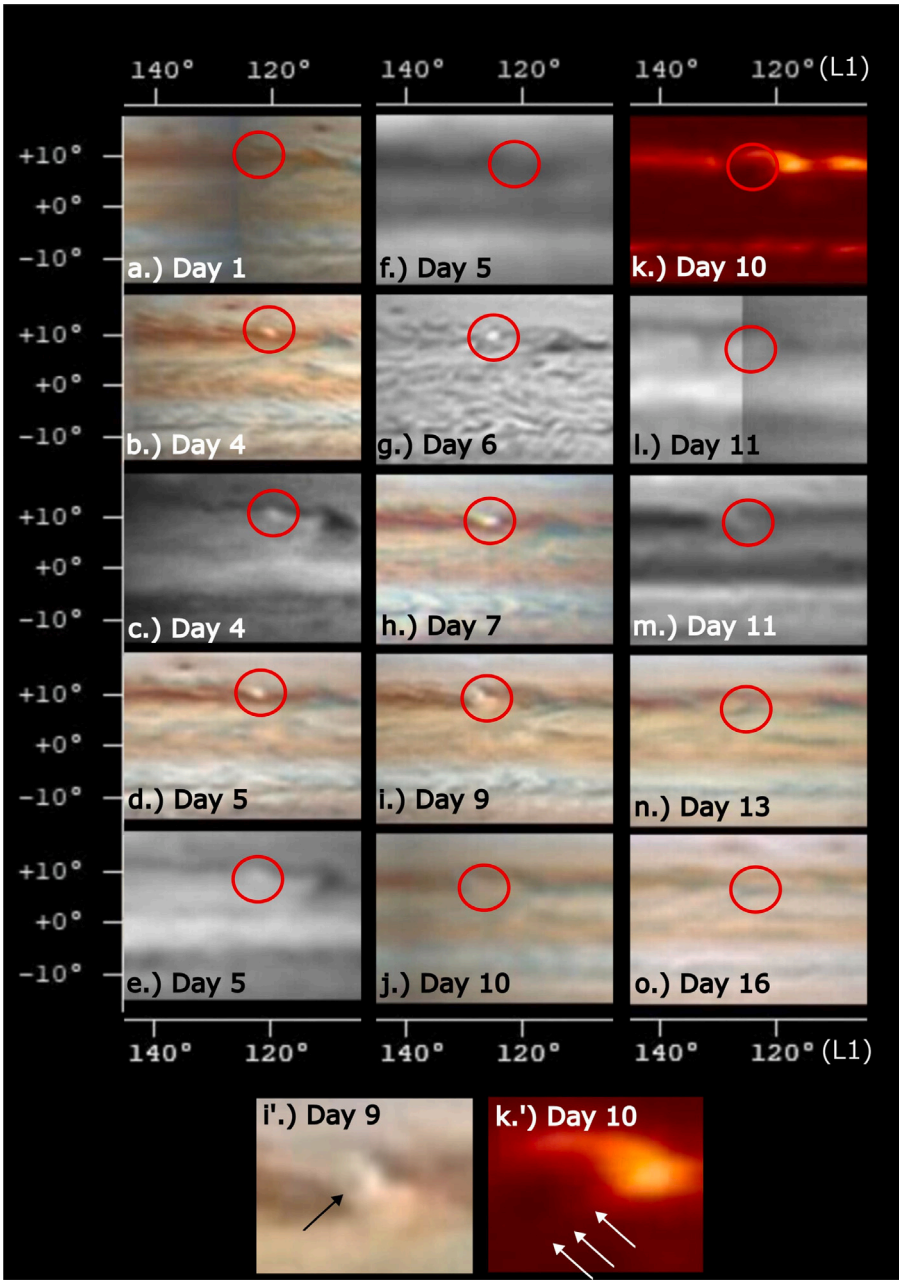


**Fig. 1.** Closeups of Earth-based image sequences of the entire Storm lifespan from Nov. 18, 2021 (Day 1) through Dec. 3, 2021 (Day 16). Circles show the approximate location of the Storm, i.e., "spot 6" in Fig. 2. RGB filtered images: Panels a, b, d, h, i, j, o. Near-IR images: Panels c, e, & l (890 nm); g (> 685 nm), Panel k (5.1-μm:). UV: Panels f & m (360 nm). Arrow in Panel i' points to a darker region just west of the bright Storm core. Arrows in Panel k' point to the faint 5.1 μm-bright festoon-like feature oriented NE to SW.

orange veil of hazes over them. It is not clear if this is the case and they could, in fact, be at a lower altitude than the bright white core.

The overall morphology of the Storm bears resemblance to terrestrial MCCs, a type of thunderstorm organization favorable in generating the observed size and duration of the PJ38 Storm (e.g., Hueso et al., 2002). MCCs, as defined for Earth, are composed of clusters of thunderstorms, which create a large anvil cloud of low eccentricity (minor/major axis >= 0.7), with temperatures <= −32 °C spanning at least 100,000 km$^2$, and temperatures <= −52 °C spanning at least 50,000 km$^2$. These size criteria must hold for at least six hours (Maddox, 1980). An example is shown in Fig. 3c. Such criteria have not been established for Jovian MCCs, and we are not proposing to do so here without a more thorough analysis of previous storms on Jupiter. It is clear, however, that the Storm's areal coverage, duration, and cloud top temperatures easily meet the terrestrial definition of an MCC. MCCs on Earth are often associated with both temperature fronts and drylines. It is the low eccentricity of the Storm cloud's top and its long duration that makes the comparison to terrestrial MCCs most apt. The patchiness of the core region (Fig. 3b, item 4b) suggests a multicellular structure, consistent with an MCC. Such patchiness can often be seen in terrestrial MCCs too.

JunoCam captured seven images of the storm in RGB filters spanning < 14 min between the extremely foreshortened first and last images of the sequence. There were no methane filter images captured of the Storm by Juno, which prevents us from estimating the heights of the clouds during the spacecraft overpass. The only methane filter images were taken from Earth about a week prior to Juno's perijove on Day 12 (Figs. 1c and 1g). An attempt was made to show if any motion

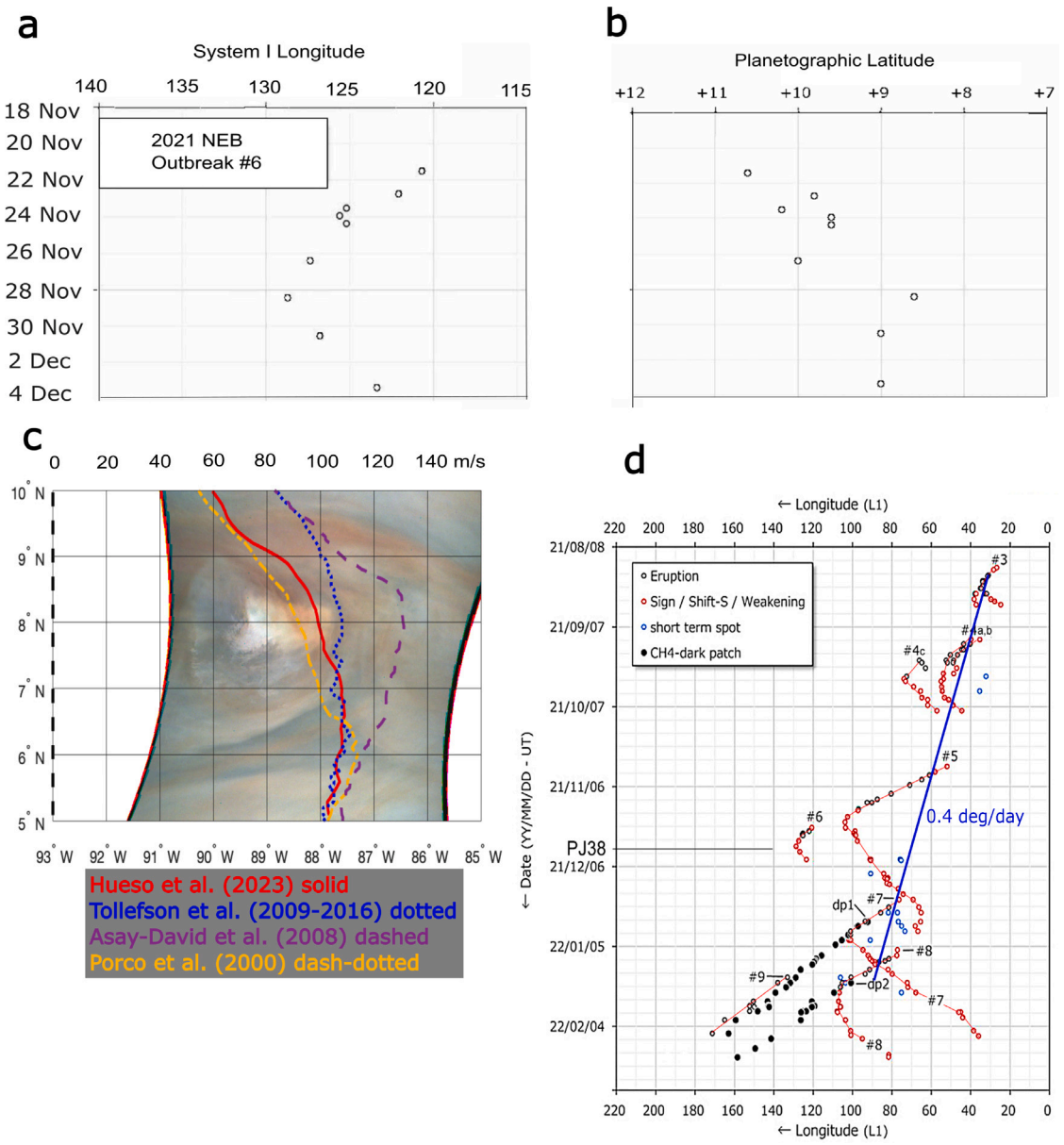


**Fig. 2.** (a) PJ38 Storm (Spot 6) drift map in System I longitude. (b) PJ38 Storm drift map in planetographic (PG) latitude. (c) Zonal wind profiles superimposed over JunoCam image of Storm. Dates refer to the year in which the data was acquired. (d) NEB(s) outbreak drift map in System I coordinates from Aug. 14, 2021–Feb. 23, 2022. Spot No. 6 (circled) denotes the PJ38 Storm.

was discernible from the RGB images. However, we were unsuccessful in this attempt due to the short temporal separation between images and parallax effects.

We include Supplemental Fig. S2 that displays JunoCam images of the PJ38 and PJ39 storms. As a note, the PJ39 storm was younger at the time of the PJ39 overpass than the PJ38 Storm. It too appears to be organized as an MCC, containing clear evidence of overshooting tops from multiple convective towers casting shadows on nearby clouds, but it lacks the translucent dispersing anvil cloud that PJ38 features west of its core.

### 2.3. JIRAM observations

The JIRAM instrument imaged the Storm over the nightside with its M-band (4.8-μm) filter. As shown in Fig. 4a, the opaque core (items 4, 5, & 6) appears as a pronounced dark 'notch,' with brighter regions appearing to the north and west (item 1), and east-northeast (item 3; see also Fig. 1k for a similar Earth-based 5-μm image). These bright features are segments of the warm NEB(s) due to low cloud opacity, allowing thermal radiation from the deeper layers of the atmosphere to escape. The festoon-like feature (item 2) is located to the south-southeast of the Storm core and running northeastward, connecting to the extended bright NEB(s) segment (Item 1). A pronounced dark "gap" appears as item 7. The global map of JIRAM images is presented as Supplemental Fig. S3, giving context to the unusual state of the NEB. Typically, the NEB appears in 5-microns as a bright wide band, and as a dark wide band in the visible. Here, the entire NEB has been reduced to a very narrow latitudinal span only a few degrees wide.

#### 2.3.1. Superimposed JIRAM and JunoCam images

Anti-correlation between RGB and 5-μm brightnesses reveal regions of optically thick clouds located at an altitude above the ~5 bar pressure level, often associated with convective upwelling. Using the best resolution JunoCam image of the Storm and a JIRAM image of the same region (Fig. 4a) we located the Storm in the JIRAM image as shown in Fig. 4b. These images are taken 4 h 34 min apart, and thus

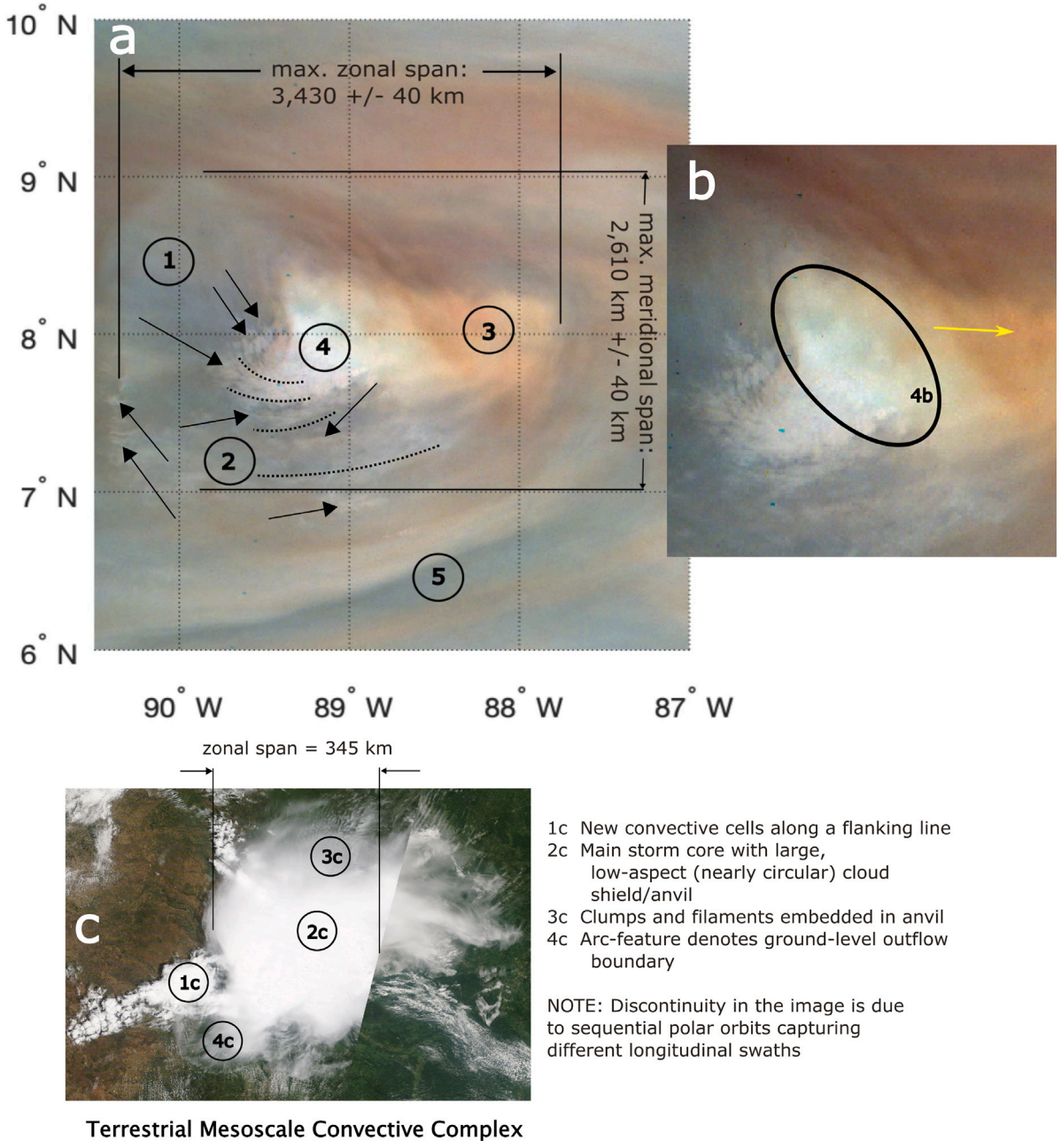


**Fig. 3.** Panel a: JunoCam image JNCR_2021333_38C00030_V01 NASA/JPL-Caltech/SwRI/MSSS/ taken at 14:22:42 UTC and subsequently reprocessed to 3 km/pixel. Item 1: Thin dispersing cirrus cloud shield/anvil. Item 2: Thin clumps & filaments embedded within the cirrus shield denoted by arrows. Item 3: Red hazes overtop presumably convective cells. Item 4: Bright Storm core featuring clumps & filaments denoted by arrows to the W and SW of the core; dashed lines showing possible anticyclonic curvature drawn parallel to cloud filaments. Item 5: Blue-gray festoon-like feature. Panel b: Close-up of Storm showing the core (4b), which contain the brightest clouds. Arrow denotes direction to the Sun. Panel c: Terrestrial Mesoscale Convective Complex (MCC) over Oklahoma, United States, July 10, 2020 (NASA, 2023). The discontinuity is due to sequential polar orbits composing the image. Item 1c: New convective cells. Item 2c: Main Storm core with large low-aspect (nearly circular) cloud shield/anvil. Item 3c: Clumps & filaments embedded in anvil. Item 4c: Arc-feature denotes ground-level outflow boundary.

we expect little evolution in the Storm morphology during this interval. However, given the time separation between the JIRAM and JunoCam images, an estimate of the zonal wind field aids in reproducing the effect of simultaneous imaging. We used the Porco et al. (2003) zonal wind profile as an initial guide.

We found the JunoCam-bright Storm clouds and the thin cirrus shield are co-located within the dark 'notch' in the JIRAM image (items 4–6, Fig. 4a). The "gap" and "tail" features (item 7) matched as did the festoon-like feature (item 2). We then refined this estimate of co-located features by fitting the anti-correlation in 5-μm brightnesses and RGB dark features, shifting the JIRAM image relative to the JunoCam image from 0°to 2.5°in small increments. The best fit by eye is 1.4 degree ± 0.1 degree, equating to a zonal wind of 105.4 ± 7.5 m/s, a value between Tollefson's (Tollefson et al., 2017) and Hueso's profiles (Hueso et al., 2023) shown in Fig. 2c. Meridional motion was not accounted for because Fig. 2b shows its drift rate is significantly smaller than the zonal motion. To the east of the white Storm core, where visibly bright clouds are tinted orange by overlying haze, JIRAM shows some patches of weak brightness, suggesting that this cloud cover is either slightly lower than the core clouds, or thinner (item 5 in Fig. 4a). The festoon-like feature (item 2) is co-located with the blue-gray arc-shaped feature in Figs. 2b and 2c. Towards the west, a long white "tail" cloud (item 7, Panel c) stretches from the southwest of the Storm westward and then northwestward to the edge of the image at 101°W, matching the

5-μm "gap" in the JIRAM image (item 7, panel a.). These 'tails' are a common feature of storms in Jupiter's belts.

### 2.4. MWR shallow channel brightness temperature maps

The microwave radiometer instrument (MWR) (Janssen et al., 2017) sounds the atmospheric ammonia and temperatures from the main cloud deck down to hundreds of bars. Fig. 5a–c details the deconvolved brightness temperature ($T_B$) maps for the three shallowest channels. We use the method of Zhang et al. (2020) to obtain the brightness temperatures (see also Section 4.4). The contribution functions of Channels 4–6 peak at 3 bar, 1.5 bar and 700 mb, respectively, well above the expected base of the $H_2O$ cloud (Atreya et al., 1999). For reference, we include an image of the Storm as revealed by JunoCam and JIRAM in panels d and f, respectively.

As the spinning spacecraft traverses over the planet, its range to the cloud tops changes along the ground track. Consequently, the MWR beam's projections on the planet ('footprints') sweep out varying sizes of ellipses with significant overlapping for a given region. This overlapping effectively samples the region and allows for a detailed brightness map to be constructed. Fig. 5e shows Channel 3's beam footprints downsampled by a factor of four for 2,000 samples that contain the Storm during the closest part of the fly over, out of a total of 141,507 footprints collected during this perijove pass.

Channel 6 (Fig. 5a) probes approximately the same altitude as the $NH_3$ condensation level (Atreya et al., 1999). South of the Storm is a region of lower brightness temperature extending north and eastward from the EZ (item 2). This lower $T_B$ 'finger' represents a higher $NH_3$ concentration surrounding a pocket of depleted $NH_3$ (warmer $T_B$) centered at ~ 5.5°N, 88.5°W (item 3), which is co-located with the 5-μm festoon-like feature (Fig. 4). To the north and east of the Storm core is a bright region centered at ~ 9°N, 87°W (item 1), which is part of the very warm NEB(s) observed in the JIRAM (Fig. 5) and IRTF images (Fig. 1k.)

Deeper, in CH.5 (Fig. 5b), a structure similar to CH.6 is evident; the core straddles a warm location to the northeast with the cool $T_B$ 'finger' to the south, and the festoon feature is still apparent (item 4 in Fig. 5f).

The contribution function for Channel 4 peaks at or slightly beneath the expected base of the $NH_4SH$ cloud layer. Here too, a similar brightness temperature structure as in CH.5 & 6 is evident. The cool $T_B$ finger is still noticeable, although the pocket of elevated brightness temperature of the festoon around 6°N, 88.5°W is no longer as easily identifiable. The bright NEB(s) north and northeast of the Storm core is still very prominent.

### 2.5. MWR deep channel brightness temperature maps

The contribution functions of Channels 1–3 peak at 240 bar, 30 bar, and 9 bar, respectively; the first two are well beneath the expected base of the $H_2O$ cloud. Channel 3 peaks slightly beneath the expected depth of the $H_2O$ cloud, depending on the local temperature and volume mixing ratio of $H_2O$ (Wong et al., 2023). Channels 1 & 2 have wider beams than Channels 3–6, i.e., 20° vs. 12°. Using the same emission-angle cutoff values as we used in the shallow channels (Zhang et al., 2020, we image a narrower set of longitudes. Fig. 6 details the deconvolved $T_B$ maps for these three deepest channels.

In CH.3 (Fig. 6a; item 2), the cool 'finger' so clearly noted in Fig. 5a–5c is barely discernible lying along the white line. Only a broad latitudinal band can be seen underneath the "hotspot" north and east of the Storm in Fig. 6b–6c (item 1 in Fig. 6b). We restricted the plotted range of $T_B$ for CH.3 to reveal the cool finger.

In the deepest two channels, the cool 'finger' is entirely absent (Figs. 6b and 6c). The regions and pockets of warm and cool $T_B$ arranged along a SSW-to-NE line (items 1–3 of Fig. 5) from the EZ into the NEB, which were evident at shallower depths, are largely gone or are unresolved by the larger footprint of the CH.1 and CH.2 beams. Here, we detect only a latitudinally-aligned gradient in $T_B$. Given that the cool finger is barely discernible in CH.3 supports the hypothesis that its absence in Channels 1 and 2 is real, rather than an artifact of poorer resolution from their larger footprints.

Fig. 6e shows Channel 1's beam footprints downsampled by a factor of four for 2,000 samples that contain the Storm during the closest part of the fly over, out of a total of 141,507 footprints collected during this perijove pass.

#### 2.5.1. Lightning sferic detections

Sferics, i.e., radio lightning detections, were observed with MWR Channels 1–3 as large antenna temperature anomalies (Brown et al., 2018; Oyafuso et al., 2020). Fig. 7 shows a JunoCam image with the MWR footprints during the times that sferics were observed in the neighborhood of the Storm. See Supplemental Fig. S4 for a complete cylindrical map showing all MWR lightning sferics for PJ38. Sferics can be located anywhere within an MWR footprint at the time it was detected. However, despite some of the CH.1 and CH.2 footprints being as large, or larger than the Storm during some of the sferic detections in the ~ 2-hr periapse encounter, it is clear from the global maps that there is a concentrated locus near the Storm, clearly demonstrating it was an active thunderstorm complex. The three sferics detected for Channel 3 during PJ38 were all located close to the Storm itself. We note that JunoCam did not reveal lightning as the Storm was in the bright dayside of the planet and the imager was not set for a short enough exposure to capture lightning flashes. Nor is lightning detectable from amateur imaging. JIRAM also did not reveal lightning as it is not sensitive to such emissions. The Waves instrument (Kurth et al., 2017) did not conclusively detect lightning that can be ascribed to the Storm, although a few detections are suspiciously close in time to MWR signals. A detailed analysis with the Waves data has not been conducted but typically, the Waves instrument does not detect many lightning signals at low latitudes as the magnetic field lines connecting it to the Storm source region were probably inaccessible (personal communication).

The spacecraft is spinning at 2 rpm along an axis that is not oriented parallel to latitude lines. Consequently, as the spacecraft approaches (departs) Jupiter over the northern (southern) polar region, the beam's footprint spans a considerable portion of the planet and can be truncated by the planet's limb. Close to the perijove latitude the footprint of each beam spans a much smaller portion of the planet, often approaching a near circular profile.

The ensemble of MWR footprints overlapping the area within a degree of latitude and longitude from the bright Storm core were integrated over 294.5 s in total. Within this sample, 15 individual sferics associated with the Storm were detected, including seven detections from CH.1, seven from CH.2, and three from CH.3 (including two simultaneously detected in Channels 2 and 3). Note, Channels 2–6 are co-bore-sighted, which means a simultaneous detection in Channels 2 and 3 will be located as the same point. Two sets of two detections each were temporally separated by only 100 ms, the lower limit that the MWR instrument can measure. If multiple lightning discharges occurred within 100 ms, as suggested by detections of dispersed pulses with submillisecond duration by Juno/Waves (Imai et al., 2020), they would be interpreted as a single pulse by MWR. Additionally, because the spacecraft is spinning, the MWR beams are not on the planet for most of the spin period, making any lightning discharges occurring during that part of the spin period undetectable. The average-weighted areal MWR footprint coverage during the 294.5 s observation period was $4.416 \times 10^7$ km$^2$. We compute a lower limit of the Storm flash rate as 0.036 flashes km$^{-2}$ yr$^{-1}$ (number of sferics/areal coverage times the observation period), a value about half the flash rate of 0.061 km$^{-2}$ yr$^{-1}$ estimated from 11 storms detected in the subpolar regions by the Stellar Reference Unit camera during seven perijoves of the Prime mission (Becker et al., 2020). If we assume all 15 sferics are localized to the Storm's larger (smaller) Storm areal coverage of $5.6 \times 10^6$ km$^2$ ($1.0 \times 10^6$ km$^2$), i.e., the outermost (inner) black curve in Fig. 5a–d, f

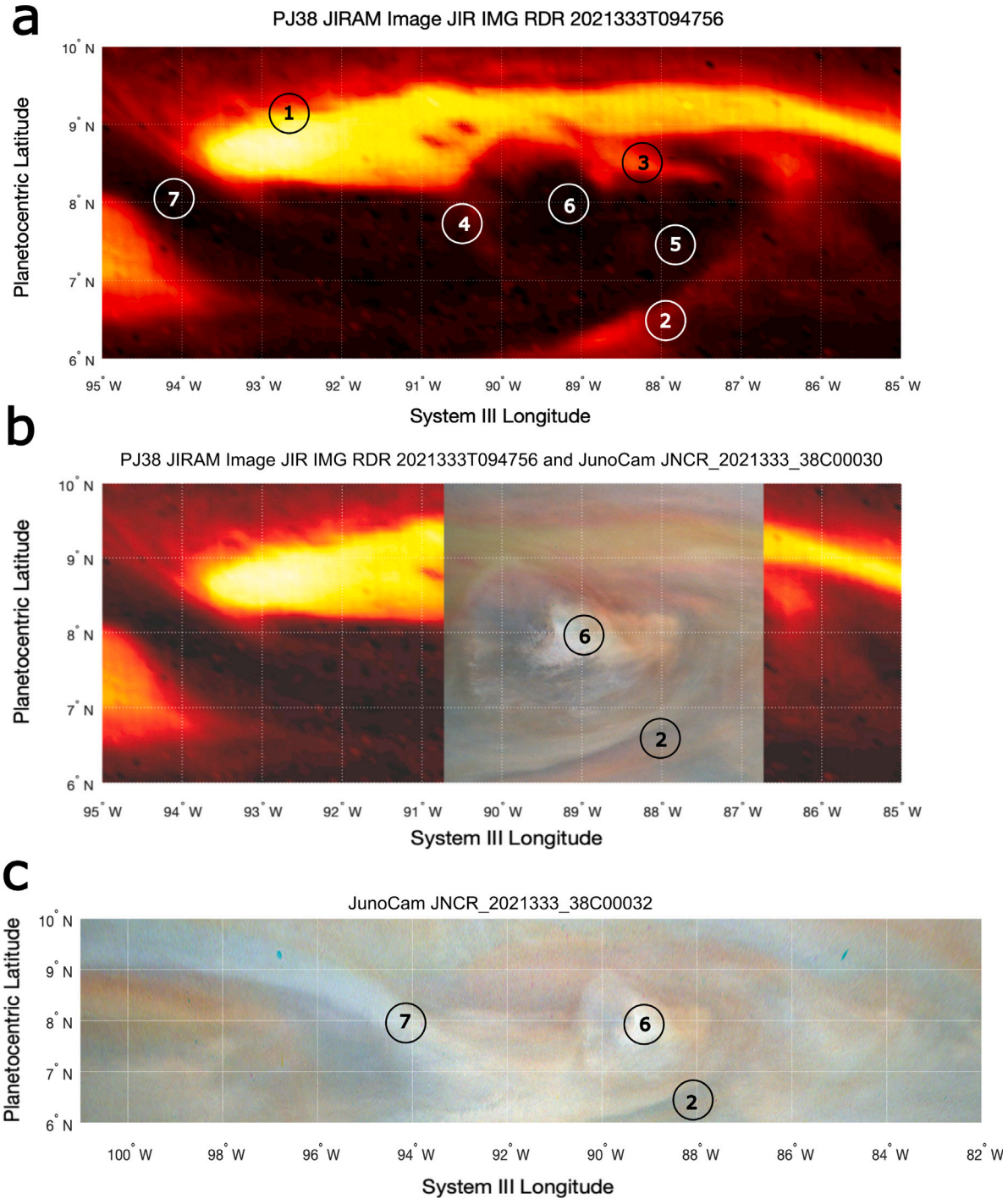


**Fig. 4.** Panel a: JIRAM image at a resolution of ~ 40 pixels/deg taken at 09:47:54 UTC and shifted by 1.4 degrees in longitude to account for temporal differences with the JunoCam images. Item 1: Atypical 5-micron hotspot spanning a narrow latitudinal range. Item 2: Festoon (arc-shaped feature connecting to 5-micron hotspot. Item 3: Thinner clouds in the 1–5 bar pressure level co-located with JunoCam red hazes east of Storm core. Item 4: Approximate edge of translucent Storm anvil west of the Storm core. Item 5: Slight brightness left of marker may signify slightly lower cloud tops or reduced opacity in the 1–5 bar pressure level. Item 6: Storm core center. Item 7: 5-μm "gap" corresponding to JunoCam bright "tail". Panel b: Superimposed JunoCam image #30 and JIRAM image. The latter has been shifted in longitude by 1.4 deg to account for temporal difference between the images. Panel c: JunoCam image #32 showing a broader range of longitudes with a reduced color stretching applied.

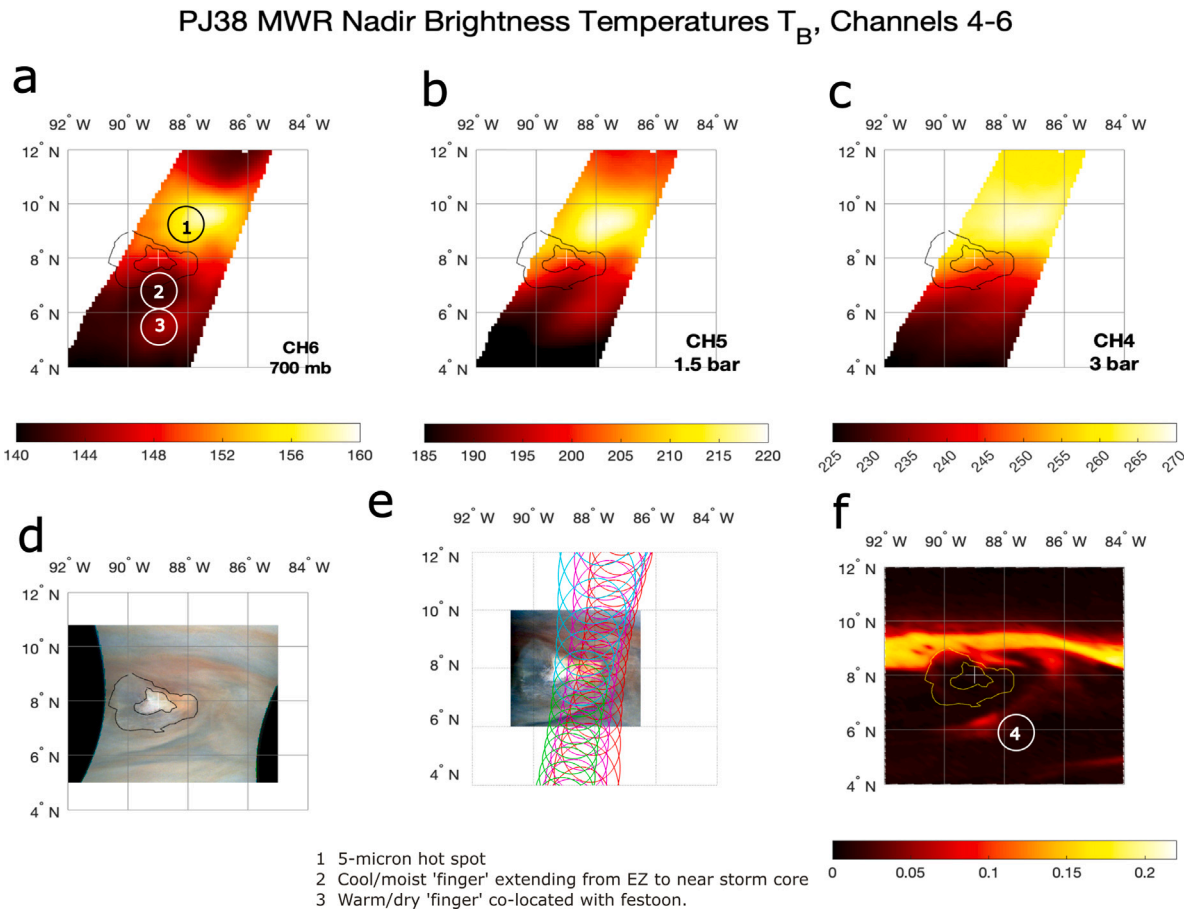


**Fig. 5.** Deconvolved MWR Brightness Temperature Maps, Channels 6, 5, and 4 (a–c). JunoCam (d), Down-sampled selection of Channel 3 footprints near closest approach to the Storm (e), color-coded simply for visibility, and JIRAM image (f). Equal-area cylindrical projections. Curved black lines in panels a-d and yellow in panel f show the outline of the anvil and bright clouds of the PJ38 Storm complex as revealed by the JunoCam image (areal extent of $5.6 \times 10^6$ km$^2$. The innermost black curve defines the Storm core of areal extent $1.0 \times 10^6$ km$^2$). Colorbars are temperature Kelvin for panels a–c, and spectral radiance W m$^{-2}$ sr$^{-1}$ μm$^{-1}$ for panel f. (For interpretation of the references to color in this figure legend, the reader is referred to the web version of this article.)

and 6a–d,f), then the flash rate increases to 0.29 (1.6) km$^{-2}$ yr$^{-1}$

Ascribing lightning detections to a particular Storm rather than to footprints that clearly contain a given feature is the approach taken by Wong et al. (2024) in their analysis of Channel 1 lightning detections from the MWR instrument. Their study focused on several storms spanning this time of unusual behavior of the NEB in 2021–2022: PJ38 (this Storm), PJ39, PJ44, and PJ47. They found that the PJ38 Storm had the lowest flash rate and a weak median equivalent isotropic radiating power compared to the other three storms. This is not a surprise as the PJ38 Storm was probably in a mature-to-decaying phase during the Juno flyover as Earth-based images show a dramatic decline in the Storm's coherence starting the very next day (Day 13, Fig. 1 m and Rogers (2021c)). As a comparison, they found the PJ39 storm to be the strongest of the four for the equivalent isotropic power, with a flash rate twice that of the PJ38 Storm.

MWR lightning detections are not correlated with depth in the atmosphere unlike detections from visible light or near-IR cameras, so no additional atmospheric structure is discernible from this data alone.

## 3. Discussion

### 3.1. The PJ38 storm MCC: A weather layer-only phenomenon

Some discrete atmospheric features such as the Great Red Spot (GRS) and other vortices (Bolton et al., 2021), and the temperate belts and zones (Fletcher et al., 2021) show $T_B$ inversions—a reversal from warm or cold in shallow-sounding channels, to cold or warm in the deep-sounding channels. For the PJ38 Storm, on the other hand, we see no evidence of a $T_B$ inversion, suggesting that it is a weather-layer phenomenon, involving only the atmosphere above the expected base of the $H_2O$ clouds.

If moisture was supplied by a plume originating beneath the $H_2O$ cloud base, perhaps as a part of an ascending branch of a Ferrell-like cell (Fletcher et al., 2020; Duer et al., 2021), or other mechanism, then such a moisture-rich plume is not evident (Fig. 6b, 6c) because we do not observe a localized $T_B$-dark anomaly associated with adiabatic cooling underneath the Storm. The beam width of CH.1& CH.2 (20°), as projected on the planet, is 1.67 times greater than those of CH.3–CH.6 (12°), which could smear out any small $T_B$ anomaly in these lowest two channels. However, the fact that the CH.3 map does not show such an anomaly with its higher resolution, and also barely shows the $T_B$-cool 'finger' structure at this depth, supports our finding that this disturbance was contained within the weather layer. If air were ascending from deep below and supplying moisture to the Storm, then its presence in the $T_B$ maps must have been perfectly masked, i.e., ascending air temperature changing precisely in opposition to any moisture change in order to maintain a constant $T_B$ compared to its immediate surroundings, which we suggest is unlikely.

We also do not observe a definitive $T_B$ anomaly beneath the Storm core or the cells to the east within the upper weather layer channels. There are two probable reasons for this. First, the footprints of Channels 3–6 are probably too large to capture the $T_B$ differences among multiple small-scale cumulonimbus towers, which have of an estimated width of $\mathcal{O}(10 - 100)$ km. Thus the observed $T_B$ is merely an 'average' of the

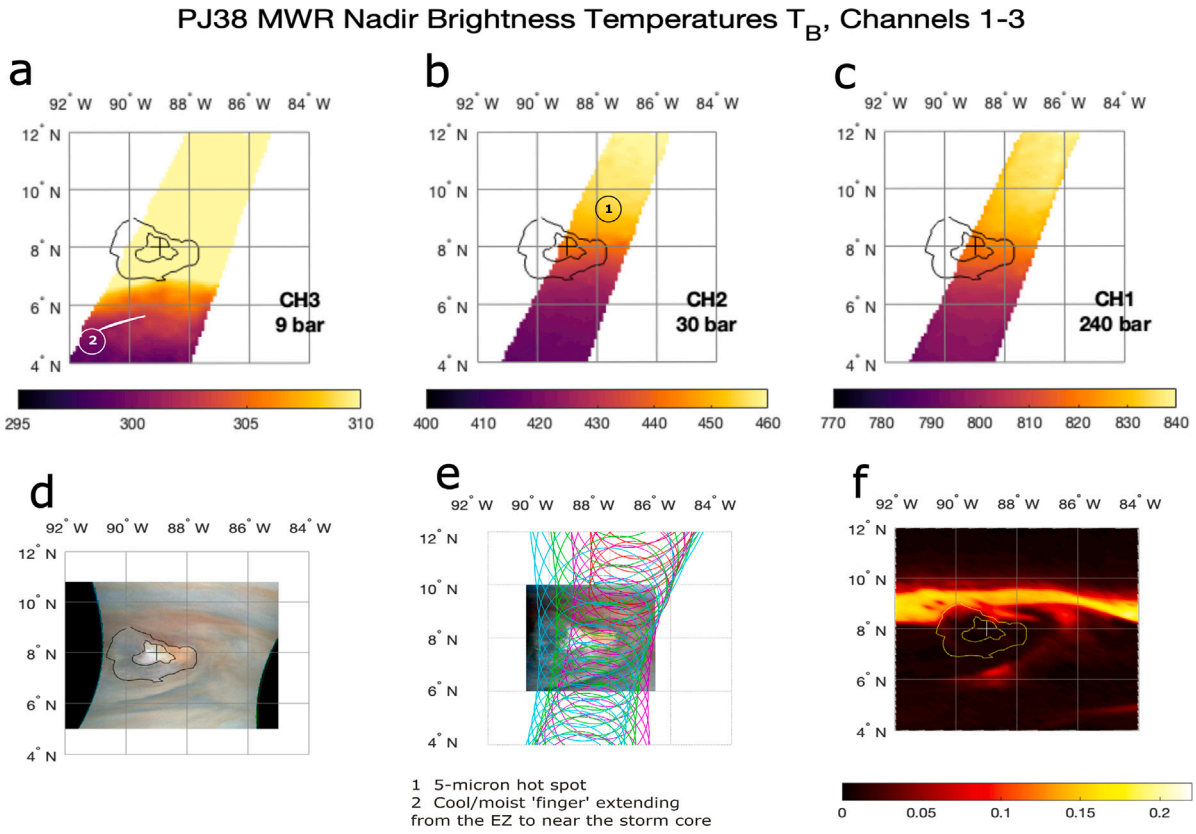


**Fig. 6.** Deconvolved MWR Brightness Temperature Maps, Channels 3, 2, and 1 (a–c). JunoCam image (d), Down-sampled selection of Channel 1 footprints near closest approach to the Storm, color-coded simply for visibility (e), and JIRAM image (f). Equal-area cylindrical projections. Curved black lines in panels a-d (yellow in panel f) show the outline of the anvil and bright clouds of the PJ38 Storm complex as revealed by the JunoCam image (areal extent of $5.6 \times 10^6$ km$^2$. The innermost black curve defines the Storm core of areal extent $1.0 \times 10^6$ km$^2$). Colorbars are temperature Kelvin for panels a–c, and spectral radiance W m$^{-2}$ sr$^{-1}$ μm$^{-1}$ for panel f. (For interpretation of the references to color in this figure legend, the reader is referred to the web version of this article.)

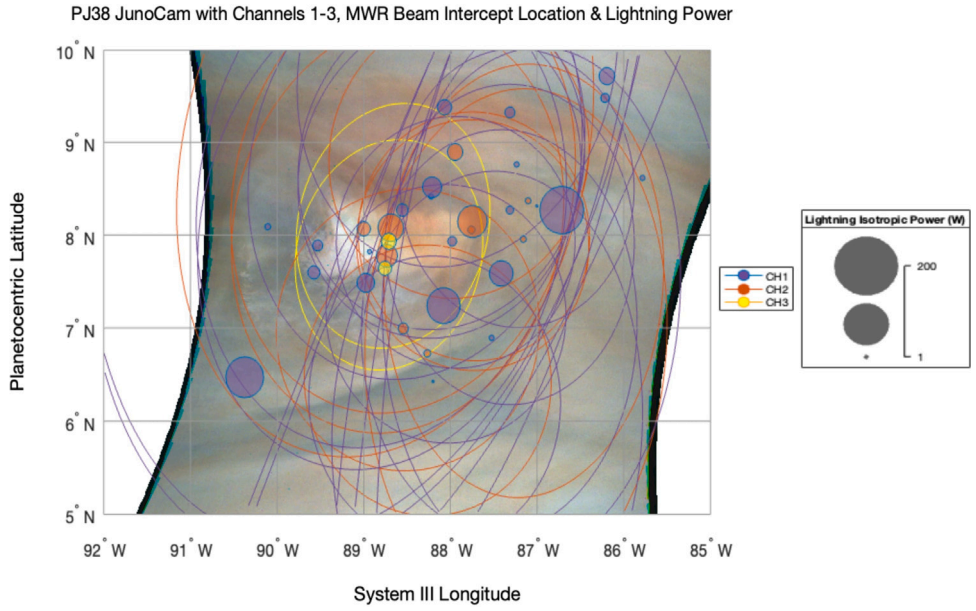


**Fig. 7.** MWR Channels 1–3 Lightning sferic footprints and isotropic power superimposed on JunoCam image. Purple, orange, and yellow curves denote CH.1, CH.2, and CH.3 footprints, respectively. Purple, orange, and yellow circles denote the center of the respective MWR footprint when lightning was detected and are linearly sized based on isotropic power. (For interpretation of the references to color in this figure legend, the reader is referred to the web version of this article.)

environment within the confines of the MCC. Second, the latent heat release lowers the amount of cooling associated with the updrafts, which reduces the difference in $T_B$ to a few Kelvin relative to the surrounding environment. Therefore, the combination of the small difference in $T_B$ between the storm towers and surroundings, and footprints larger than the storm towers makes it unlikely that a definitive $T_B$ anomaly associated with Storm updrafts would be detectable.

The PJ38 Storm appeared to be organized as a MCC, particularly during Days 1–12. The brightest clouds of the Storm core meet the terrestrial requirements of areal extent and low cloud-top horizontal eccentricity defining an MCC (east–west vs. north–south cloud span). Hueso et al.'s 3D storm modeling results (Hueso et al., 2002) supports our finding that the PJ38 Storm was multi-cellular in nature, based on the observed cloud top areal extent and storm duration. Their results suggest storm lifetimes of only hours to a day.

The core of the Storm contains the brightest clouds and these are usually the site of the most recent convection. The thin cirrus west of the core may simply be an older anvil from a previous convective "pulse" earlier in the Storm cycle that has begun dispersing, or possibly drifting westward as it has risen to a higher altitude where the zonal wind speed is expected to be reduced. The bright orange-tinted clouds east of the core are probably also convective cells, but whether they are older or younger than the core cells is not certain. Their orange color appears to be due to an overlying orange haze, aligned from northwest to southeast.

### 3.2. The climate of the NEB

The NEB is a region often punctuated with bright storm clouds and multiple rifts and plumes (Fletcher et al., 2020) like the one investigated in this paper, which are assumed to be thunderstorms. Interestingly, previous MWR-analyses show the NEB as a region that features a strong latitudinal gradient of $NH_3$ abundances (Li et al., 2017). If $H_2O$ abundance distribution in the NEB is also subjected to a similarly strong gradient, then we may have a region that is climatologically favorable for thunderstorm formation, which matches the observations of the stormy NEB dating back to the Voyager epoch.

Gradients in $H_2O$ vapor abundances (humidity) on Earth are often associated with MCC outbreaks, like those in North America, or in the Sahel region of Africa in summer. The mixing of moist and dry airmasses of nearly identical temperature along a narrow humidity gradient ('dryline'), is favorable for thunderstorm formation, including those in MCCs (Markowski and Richardson, 2010; Bluestein and Parker, 1993). On Jupiter, an $H_2O$-rich air mass originating in the EZ may be stable to convection because its greater molecular weight can support an otherwise unstable superadiabatic lapse rate (Cheng et al., 2024). Mixing this air with drier air from the NEB through small-scale turbulence, parcel motion, and entrainment (as on Earth) may be enough to reduce the molecular weight suppressing effect and make the superadiabatic lapse rate highly unstable to convection. A thunderstorm outbreak would be a likely outcome.

The NEB's cyclonic environment is favorable for the development of thunderstorms. Several authors (Thomson and McIntyre, 2016; Dowling and Gierasch, 1989; Fletcher et al., 2017; Fletcher et al., 2020) have postulated that the air in the cyclonic belts feature a relatively short vertical distance from the $H_2O$ lifting condensation level (LCL) to the level of free convection (LFC). This concept is also supported by the isentropic potential vorticity perspective (IPV) of cyclonic regions (Hoskins et al., 1985; Allison, 2000), which states that isentropes bulge upward in the lower part of the weather layer. As air flows along these isentropes it ascends and cools, becoming favorable for releasing potential instability, i.e. lifting a layer of stable air such that the entire layer becomes conditionally unstable (Holton, 2004), a common mechanism on Earth for destabilizing air.

Any additional mesoscale forcing promoting lift and condensation, such as from a dryline, could more easily set off a convective outburst. The formation of a dryline could be the result of an underlying disturbance generating flow with a meridional component thereby forcing EZ and NEB air together along a narrow region. We note that the mechanism behind what forms or supports the disturbance itself is unclear but could be tested with appropriate non-hydrostatic modeling and continuing long-term observations of Jupiter's belt-zone interfaces.

Sugiyama et al.'s models (Sugiyama et al., 2011, 2014) show prolonged periods of quiescence exist during which convective available potential energy (CAPE) builds. A 'cap' of stable air is required for this to occur, as is the case on Earth. The belt-zone stacked-cell hypothesis suggests that air flows from zones to belts in the upper troposphere (Ingersoll et al., 2000; Fletcher et al., 2020) and subsides over the belt. Adiabatic compression from subsidence creates the cap as a warmer and presumably convectively stable layer. In Sugiyama's models, downdrafts from aerosol evaporation eventually perturb the air at the $H_2O$ layer sufficiently to reach their LFCs initiating their modeled 2–4 day active storm period. Interestingly, however, our observations show a much longer active period than the models do, which supports the hypothesis that additional forcing is occurring to prolong this Storm.

The exceptional quiescence and whitening of the NEB in 2021 was a type of phenomena that Sugiyama's models could help explain. In this case, however, the storm outbreaks that would terminate the NEB fade were restricted to the NEB(s), the only part of the belt that had not been covered by high-albedo clouds. We suggest that at this latitude, the convergence of $H_2O$-rich equatorial air, build-up of CAPE in the NEB, and a disturbance promoting advection of airmasses and the formation of a dryline, led to outbreaks such as the PJ38 Storm.

The isolated convective activity at a drifting longitude in 2021 supports the stealth superstorm scenario (Fig. 2) (Rogers and Mizumoto, 2022; Wong et al., 2023). Our analysis of MWR data in Channels 1–3 argues against a localized thermal or compositional anomaly originating below the weather layer as the triggering mechanism.

### 3.3. Mesoscale-to-storm scale mechanisms for forming and sustaining the PJ38 storm

In this section we propose a scenario that supports our hypothesis that a dryline was involved in forming or maintaining the 2-week lifespan of the Storm. It is not the only plausible scenario but does fit the data. Here, we expound on more on the ideas presented in Section 3.2. Non-hydrostatic models tuned for Jupiter can provide insight to the mechanisms and can test if such a dryline could form and support such a Storm. Therefore, we provide this section in the hopes it will guide future modeling efforts while also explaining our interpretation of the data and the mechanisms involved. We must rely on modeling studies as we have no in-situ measurements of any Jovian thunderstorm, nor will we in the foreseeable future.

Jupiter storm models (Hueso et al., 2002; Sugiyama et al., 2011, 2014) applied to individual cells and clusters of cells arranged as an MCC find storm lifetimes of only hours to a few days, much shorter than the PJ38 Storm. Therefore, prolonged forcing mechanism(s) were likely responsible for sustaining the Storm (and similar long duration ones in the NEB and SEB) such as from temperature fronts, drylines, and gust fronts. These mechanisms are not mutually exclusive and could act in concert.

At the sharp temperature gradient along a front, or moisture gradient along a dryline, denser air displaces more rarefied (i.e., less dense) air upward, providing lift and often generating thunderstorms including MCCs (Bluestein and Parker, 1993; Vizy and Cook, 2018). We observe a $T_B$ gradient in the MWR maps. Previous MWR analyses (Bolton et al., 2017), however, suggest $T_B$'s are driven more by $NH_3$ humidity than temperature, particularly in Channels 1–4. If this is the case, then the cool $T_B$ finger/plume shown in Channels 6, 5, 4, and perhaps 3, result from a higher $NH_3$ humidity, i.e., a dryline. However, we must also simultaneously hypothesize that regions of high (low) $NH_3$ humidity

are correlated with high (low) $H_2O$ humidity, because it is $H_2O$ that is needed for a thunderstorm. If these assumptions are correct, then a dryline occurring within the weather layer may have been responsible for sustaining the PJ38 Storm at least for a part of its 2-week duration, and this may also have been the mechanism producing the other episodic convective eruptions at the active longitude throughout 2021 and into 2022 (Fig. 2).

Drylines in Jupiter's low molecular weight atmosphere would operate opposite to those on Earth, with moist air advecting underneath and lifting the drier air (although not completely devoid of $H_2O$ vapor). For this reason, on Jupiter, a dryline might be more properly called a 'wetline.' Fig. 8a is schematic of the initial state where denser, presumably $H_2O$-rich air from the EZ, advects into and under the drier and less dense NEB(s) air, i.e., a dryline (Fig. 8 item 1). As a result of this advection of air masses, the NEB(s) air is forced to ascend isentropically along the dryline and cools, priming the atmosphere for potential instability (Fig. 8, items 2 and 4). An additional source of moisture for the dry NEB(s) airmass may come from moist air parcels seated deep in the weather-layer being perturbed upward, entraining drier air, and subsequently mixing the air parcels (Fig. 8b items 5 and 6). This mixing moistens the air, further priming the air for conditional instability, which would be later released when vapor condenses into clouds (e.g., Del Genio and McGrattan, 1990). On Earth, a similar situation commonly arises as moist air parcels rise and, mix with the drier air above. This moistening erodes the convective suppressing 'cap' layer, making it more likely that a new parcel will break through the stable cap and reach its LFC.

As Sugiyama's and Del Genio's models suggest, a similar moistening effect may take place from above. Sugiyama's modeling demonstrated that existing $NH_3$ and/or $NH_4SH$ clouds precipitate and generate evaporatively cooled downdrafts (Fig. 8b, item 5). These moist downdrafts mix the moist EZ air that advects below the NEB along the dryline with the drier NEB airmass, further promoting erosion of a stable cap. Simultaneously, the EZ air near the dryline dries from mixing with the NEB air. As a result of this drying, the stabilizing effect of the presence of a high molecular weight vapor gradient effect is reduced or eliminated altogether. Downdrafts reaching the $H_2O$ LCL spread horizontally, per Sugiyama's models, inducing new updrafts. The new updrafts form shallow cumulus clouds that will, in turn, begin to precipitate (Fig. 8b, item 5). The mixing–moistening cycle is thereby enhanced, favoring new cumulus cells to reach the $H_2O$ LFC. At this point, a thunderstorm cell is imminent.

The nascent thunderstorm cell is joined by additional cells and forms the MCC, whose cloud tops reach the upper troposphere, becoming visible to earth-based and Juno spacecraft observations (Fig. 9a). The multiple cells that comprise an MCC are all in varying stages, i.e., formation, maturation, and dissipation. The collective effect is a large region of active thunderstorms lasting far longer than any single thunderstorm cell would last. Fig. 9b details a cross-sectional schematic of this MCC along line A–B of Fig. 9c. Panels c–h of this figure shows a vertical arrangement of the JunoCam and MWR plots from Figs. 5 and 6 looking towards the northwest.

The downdrafts from the MCC might organize into gust fronts. Gust fronts, particularly those that organize into a dominant line, are important in terrestrial convection in generating new cells and thus greatly prolonging the duration of a storm (Lin and Joyce, 2001; Schumacher and Rasmussen, 2020). Sugiyama et al.'s 2D numerical results suggest the $H_2O$ LCL (Fig. 9b; here shown at 9 bar but probably varies by 1–2 bar) acts as a dynamical boundary, posing an attractive model for how gust fronts might operate on Jupiter. During the most violent part of the cycle in their models, downdrafts of $\sim 50$ $ms^{-1}$ or more rapidly slowed to zero at the LCL. If downdrafts cannot penetrate the $H_2O$'s LCL, as Sugiyama et al.'s models show (Fig. 9b, item 4), then perhaps they are forced to spread horizontally, lifting new parcels and generating new cells (Fig. 9b, item 5). The cells to the east of the Storm core may be in the direction of these gust fronts. Furthermore, we envision a stable LCL rippling with gravity waves as the downdrafts impinge, creating additional lift at the wave crests. While Sugiyama et al.'s LCL dynamical boundary is an attractive answer for how gust fronts may propagate and sustain storms for prolonged periods, it needs confirmation with appropriate 3D non-hydrostatic modeling.

Another dynamical dimension is provided by east–west velocity shear with respect to latitude. Usually the 'hotspots' and 'festoons' on the south edge of the NEB, believed to be manifestations of equatorial Rossby waves, drift eastward at ~100 m/s (Rogers, 2019a). In 2021, concomitant with the quiescence of the NEB, these all disappeared and were replaced by smaller features moving rapidly eastward at ~130–145 m/s (Rogers et al., 2022; Rogers, 2021c). Conversely, the superstorm and the initial storm outbreaks within it, moved at less rapid velocities of ~105 m/s, typical of their latitude at 8–9°N. At PJ38, the 'cool/moist finger' from the EZ, lying between the small festoons which were probably moving at the very fast rate, may have been moving past the superstorm at ~40–68 m/s (2–4 degrees longitude per day). Each individual storm during 2021 may have been induced in a 'hit-and-run' manner by such 'cool/moist fingers', and then self-propagated as previously suggested.

## 4. Methods

### 4.1. Earth-based observations

Nearly all of the Earth-based observations are from amateur astronomers and NASA's Infrared Telescope Facility (Rayner et al., 2003). These observers uploaded their images to the Association of Lunar and Planetary Observers in Japan (ALPO-Japan; http://alpo-j.sakura.ne.jp/indexE.htm). The images are then map-projected and made publicly available. We downloaded the appropriate maps that captured the Storm and made our figures from these maps. Portions of Fig. 2 were also provided by ALPO-Japan.

### 4.2. JunoCam

We used the Integrated Software for Imagers and Spectrometers (ISIS) (USGS-Astrogeology, 0000) and NAIF SPICE kernels (Acton, 1996) to process JunoCam images from the Planetary Data System's (PDS) Atmosphere Node (Caplinger, 2016). LINUX command-line scripts were used to execute the following ISIS commands in order: *junocam2isis* → *spiceinit* → *cam2map* → *photomet* → *phocube* → *automos* → *cubeit*. We projected the image and associated latitude–longitude data on a cylindrical map with a resolution of 3 km/pixels. Our estimate of the size of the Storm is based on an error of 10 pixels (~30 km) since the location of the Storm cloud edges is somewhat subjective. RGB images produced in the final step were opened and inspected in ISIS's *qview*. We then traced curved lines that defined the Storm perimeter and the Storm core using *qview*. The images, their associated latitude–longitude data, and the polylines were then exported in ASCII form for color stretching, contrast enhancement, and plotting with MATLAB's Mapping Toolbox functions.

### 4.3. JIRAM

We used SpiceyPy (Annex et al., 2020) to process JIRAM images acquired from the PDS Atmosphere's Node and their associated SPICE kernels (Noschese and Huber, 2019). We then exported the images and their associated latitude–longitude backplane data for color stretching and plotting on a cylindrical map at the image resolution of ~20 pixels per degree using MATLAB's Mapping Toolbox functions.

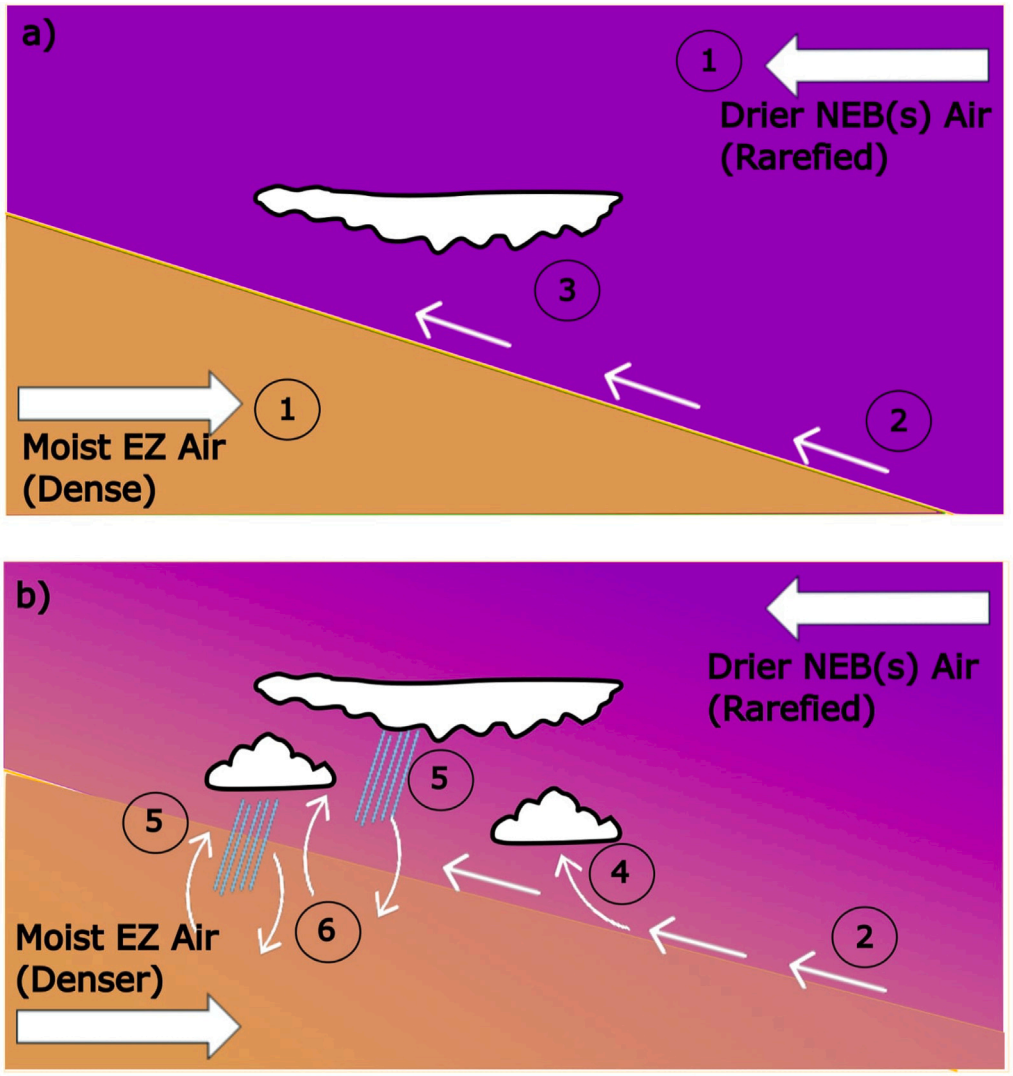


**Fig. 8.** Panel a): Initial state of dryline. (1) Advection of moist, dense, $H_2O$-rich air from the EZ (orange color) under the drier, more rarefied NEB(s) air (violet color). (2) NEB(s) air isentropically ascending and cooling. (3) $NH_3$ and/or $NH_4SH$ clouds initially present or forming. Panel b): Intermediate state of the dryline, thunderstorm outbreak imminent. Along the dryline boundary, mixing of air moistens the NEB(s) air while drying EZ air, represented by the color gradient. Items (1) and (2) as before. (4) Isentropic uplift and small-scale turbulence mixing the EZ and NEB(s) air allowing for $H_2O$ reaching its LCL, forming $H_2O$ clouds. (5) Precipitation from existing clouds creating downdrafts, (6) further mixing and perturbing EZ and NEB(s) air allowing for additional $H_2O$ cloud formation and vertical uplift to the LFC. (For interpretation of the references to color in this figure legend, the reader is referred to the web version of this article.)

#### 4.3.1. JunoCam-JIRAM superimposed

Knowledge of the zonal wind field is useful to reproduce the effect of simultaneous imaging with JunoCam and JIRAM. These images were taken 4 hr 34 min. apart in a region where cloud-top zonal winds are typically ~ 100 $ms^{-1}$. We estimated the displacement using the Cassini zonal wind profile (Porco et al., 2003) for the Storm's core latitude of 8°, shifting the JIRAM image relative to the JunoCam image (Fig. 3e). We then refined this estimate of co-located features by fitting the anti-correlation in 5-μm brightnesses and RGB dark features, shifting the JIRAM image relative to the JunoCam image from 0° to 2.5° in small increments.

Meridional motion was not accounted for as Fig. 2 shows that component of drift is negligible relative to the zonal component and less than a single JIRAM pixel width during this short time interval. The JunoCam and JIRAM images were stacked in MATLAB with a transparency value (MATLAB's 'alpha' setting) that provided a good representation of both images simultaneously.

### 4.4. Microwave radiometer observations

#### 4.4.1. Brightness temperatures

To obtain brightness temperatures from MWR antenna temperatures, we use the model published by Oyafuso et al. (2020), and limit ourselves to emission angles < 60°. Large emission angle observations elongate the projected beam and have worse resolution. This approach allows us to fit the observations of antenna temperatures to a model, and, from this model and the emission angle of the beam, the nadir-equivalent brightness temperatures can be computed.

For each channel and each physical location that is modeled, the angular dependence of the thermal emission is formulated as,

$$\mathrm{Model}_{\mathrm{TB}}(\mu) = \epsilon(\mu)\left[c_0 - c_1\frac{1-\mu}{1-\mu^*} + \frac{c_2}{2}\frac{(\mu-\mu^*)(1-\mu)}{(1-\mu^*)^2}\right] \quad (1)$$

where $\mu$ is the cosine of the emission angle and $\mu^* = 0.8$. $\epsilon(\mu)$ is an empirical shape function accounting for deviations from a quadratic fit at larger emission angles. Values of $c_0$, $c_1$, and $c_2$ over latitudes and

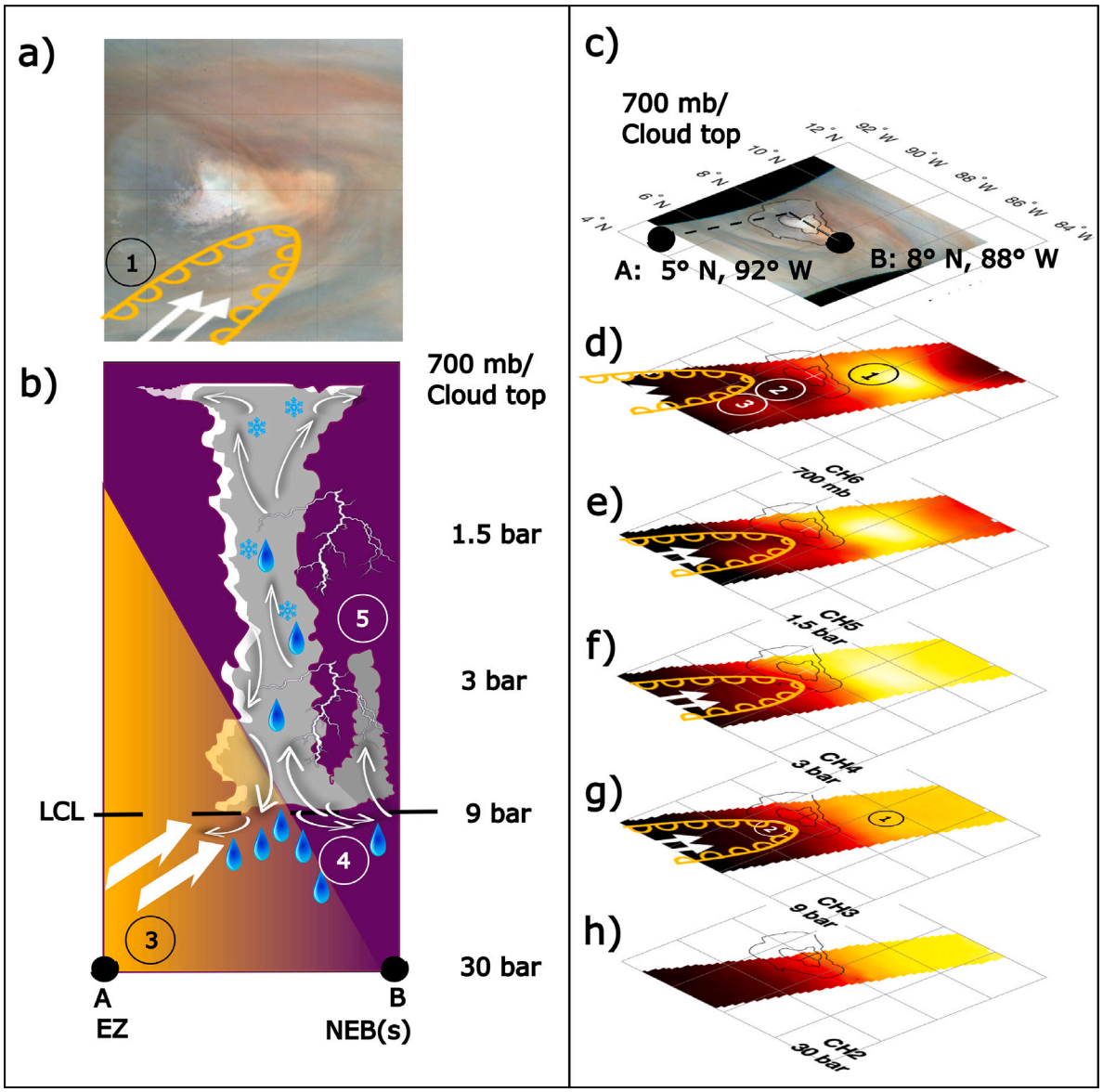


**Fig. 9.** Panel (a): JunoCam image with dryline symbol (item 1). White arrows in item 1 show air flow from the EZ into the NEB(s). Panel (b): Cross-sectional schematic of the MCC showing lightning, solid hydrometeors, liquid precipitation descending below the LCL, and a thin cirrus shield located to the west (left) of the Storm core. The double white arrow shows EZ air advecting from the SW (item 3). Downdrafts (4) spread out at the LCL, which form a gust front generating new thunderstorm cells (5). Panels (c–h): Rotated and vertically arranged panels from Figs. 5 and 6 positioned at the pressure levels shown in panel b. Note panels c and d are both most sensitive at 700 mb and shown vertically separated for clarity. Items 1–3 in these panels are as in Figs. 5 and 6.

shape functions for each of the six MWR channels are found in Oyafuso et al. (2020).

Next, this brightness temperature model, which is longitudinally averaged over multiple perijoves, is convolved with the beam to get a modeled antenna temperature:

$$T_a(\theta,\phi) = \int_0^{2\pi}\int_0^{\pi} \mathrm{Model}_{\mathrm{TB}}\left(\theta',\phi'\right) g\left(\theta'-\theta,\phi'-\phi\right)\sin\left(\theta'-\theta\right) d\theta' d\phi' \tag{2}$$

where $(\theta'-\theta,\ \phi'-\phi)$ is the angular deviation from the beam boresight direction, $(\theta,\phi)$. $T_b(\theta',\phi')$ is the brightness temperature in the direction of the solid angle element $\sin(\theta'-\theta)d\theta' d\phi'$ and $g(\theta'-\theta,\phi'-\phi)$ is the gain along the antenna boresight direction. The gain, $g(\theta,\phi)$ (Janssen et al., 2017), is normalized to a value of one over $4\pi$ sr:

$$\int_0^{2\pi}\int_0^{\pi} g(\theta,\phi)\sin\theta d\theta d\phi = 1 \tag{3}$$

This modeled antenna temperature can then be compared with observed antenna temperatures. A residual is defined as the difference between the two temperatures:

$$T_{\mathrm{resid}} = T_a^{obs} - T_a^{\mathrm{model}} \tag{4}$$

The set of residuals is a measure of how consistent the model is with the real Jupiter atmosphere. Under the assumption that the overall brightness model is close enough to the real case, the residuals can be approximated as the deviation of the real brightness temperature from the model along the boresight direction. And we update the brightness temperature for each data point by applying the following equation,

$$T_{\mathrm{best}}^{\mathrm{iter}\ 0} = T_{\mathrm{bmodel}} + T_{\mathrm{resid}} \tag{5}$$

where $T_{bmodel}$ is the brightness temperature for each observations, derived using $Model_{TB}$.

The latitudes of the measurements are grouped into one degree size bins. For each latitude bin, we plot $T_{\mathrm{best}}^{\mathrm{iter}\ 0}$ from all perijoves (using

only the data points with the beam fully on the planet) with respect to emission angles, together with the deconvolved brightness temperatures from PJ1-9. We then fit all the data to equation $Model_{T_B}^{iter1}(\mu) = \varepsilon(\mu)\left[c_0 - c_1\frac{1-\mu}{1-\mu^*} + \frac{c_2}{2}\frac{(\mu-\mu^*)(1-\mu)}{(1-\mu^*)^2}\right]$. The c-coefficients are free parameters. Outliers are removed and the fitting is applied again. This process is repeated for all latitude bins and the brightness temperature model is updated. This new updated brightness temperature model is convolved with the beam, and we obtain a new modeled antenna temperature, new residual, and a new $T_{\text{best}}^{\text{iter }1}$. This process is repeated for several iterations until the results converge. The final brightness temperature is then corrected to the nadir direction using the coefficients from the final iteration, $T_{\text{best nadir}}^{\text{final iter}}$, which is the value we use to make brightness temperature maps.

Brightness temperature maps are then produced from MATLAB's Delaunay triangulation function to linearly interpolate the 2D MWR data sets for each of the six channels.

#### 4.4.2. Lightning power

Lightning power is computed as in Brown et al. (2018). We used SPICE kernels from the PDS to find the position and slant distance along the center of the beam line to the 1-bar level.

## 5. Conclusions

A multi-instrument data set of JunoCam, JIRAM, MWR, and Earth-based images of a thunderstorm on Jupiter — the first of its kind — was obtained by Juno during the 38th perijove at close range (< 6,000 km) and with suitably low emission angles. Analysis of this data set suggests possible mechanisms responsible for explaining the morphology, evolution, and long duration of this Storm. We summarize our three key findings.

1. The bright cloud feature observed from JunoCam centered at 8°N, 89°W was a mesoscale convective complex. Lightning, the necessary ingredient to classify a cumulus cloud as a thunderstorm was present during the Juno flyover. Radio emissions obtained by the MWR instrument confirmed the Storm's strong moist-convective nature.
2. This Storm was contained entirely within the weather layer, i.e. no deeper than the base of the $H_2O$ cloud. MWR data show no $T_B$ anomaly at the Storm in channels whose contribution functions peak well below the weather layer. Such an anomaly would be expected if adiabatic cooling from a deep-seated vertically rising plume was responsible for the Storm.
3. The Storm's lifetime of ~2 weeks, and perhaps its very origin, was due to synoptic-to-mesoscale forcing mechanisms. This Storm lasted longer than a single cell, or clusters of cells based on previous simulations. The proposed forcing mechanism was probably the result of a dryline, and perhaps supported by gust fronts. This proposition is somewhat speculative, but testable with appropriate 3D non-hydrostatic models.

Observation of the PJ38 Storm, coupled with our current understanding of thunderstorm dynamics on Earth and Jupiter, suggest that Jovian and terrestrial thunderstorm dynamics may be more similar to one another despite glaringly obvious differences in the atmospheres and interiors of the two planets. The results from our observations and from previous storm modeling support our hypothesis that synoptic and mesoscale forcing mechanisms may be key to understanding storm formation and development on Jupiter as they are on Earth.

Future dynamical modeling will be required to address a number of the hypotheses and storm mechanisms presented herein. For example, does the $H_2O$ LCL truly function as a dynamical barrier for downdrafts in a 3-D non-hydrostatic model as it does in a 2-D model? In short, does the LCL essentially operate as a quasi-hard surface on Earth as far as downdrafts are concerned? Do gust fronts organize new cells and how does vertical wind shear promote or impede storm evolution on Jupiter?

Continued efforts to better separate air temperature from $NH_3$ and $H_2O$ abundances in MWR data will be extremely valuable to constrain the mechanisms influencing similar storms, as well as determining $H_2O$ abundance variations in belts and zones. New observations of Jovian storms with microwave-sensing capability from Juno (or future spacecraft) will shed light on the various environments and mechanisms forming and sustaining thunderstorms in hydrogen-dominated atmospheres. Earth-based observations will also be necessary to provide nearly continuous, global, and long-term monitoring of Jupiter, which are critical for interpreting spacecraft instrument data.

## CRediT authorship contribution statement

**Shawn R. Brueshaber:** Writing – review & editing, Writing – original draft, Methodology, Investigation, Formal analysis, Conceptualization. **Zhimeng Zhang:** Writing – review & editing, Software, Methodology, Formal analysis. **John H. Rogers:** Writing – review & editing, Resources. **Gerald Eichstädt:** Writing – review & editing, Formal analysis. **Glenn S. Orton:** Writing – review & editing. **Davide Grassi:** Formal analysis. **Leigh N. Fletcher:** Writing – review & editing. **Cheng Li:** Methodology, Formal analysis. **Shinji Mizumoto:** Resources, Formal analysis. **Alessandro Mura:** Investigation, Formal analysis. **Fabiano Oyafuso:** Methodology, Formal analysis. **Ramanakumar Sankar:** Writing – review & editing. **Michael H. Wong:** Writing – review & editing. **Candice J. Hansen:** Investigation. **Steven Levin:** Writing – review & editing. **Scott Bolton:** Investigation, Funding acquisition.

## Declaration of competing interest

The authors declare that they have no known competing financial interests or personal relationships that could have appeared to influence the work reported in this paper.

## Acknowledgments

This work was performed under a Juno subcontract to Western Michigan University from the Southwest Research Institute; at the Jet Propulsion Laboratory, California Institute of Technology, under a contract with the National Aeronautics and Space Administration. Fletcher was supported by STFC Consolidated Grant reference ST/W00089X/1. For the purpose of open access, the author has applied a Creative Commons Attribution (CC BY) license to the Author Accepted Manuscript version arising from this submission. Li was supported by the NASA Juno Program, under NASA Contract NNM06AA75C469 from the Marshall Space Flight Center supporting the Juno Mission Science team, through subcontract Q99063JAR to the University of Michigan from the Southwest Research Institute. JIRAM is funded by ASI with contract 2016-353 23-H.3 (addendum). This research has made use of the USGS Integrated Software for Imagers and Spectrometers (ISIS). The authors were Visiting Astronomers at the Infrared Telescope Facility, which is operated by the University of Hawaii under contract 80HQTR19D0030 with the National Aeronautics and Space Administration.

We thank Andrew Ingersoll and an anonymous reviewer for their valuable feedback and suggestions. We thank the legions of venerable amateur astronomers who faithfully keep a watch on Jupiter when the spacecraft and professional observatories cannot.

## Appendix A. Supplementary data

Supplementary material related to this article can be found online at https://doi.org/10.1016/j.icarus.2025.116465.

## Data availability

The Juno MWR observations used in this analysis work are available through the Planetary Data System Atmospheres Node. Data are stored in ASCII tables with supporting documentation at https://pds-atmospheres.nmsu.edu/data_and_services/atmospheres_data/JUNO/microwave.html. MWR data files can be found online at https://pds-atmospheres.nmsu.edu/PDS/data/jnomwr_1100/data_calibrated/. JunoCam and JIRAM data are available as .IMG and .LBL files at https://pds-imaging.jpl.nasa.gov/volumes/juno.html and https://atmos.nmsu.edu/PDS/data/PDS4/juno_jiram_bundle/data_calibrated/, respectively. Amateur and IRTF 5-micron images can be found at https://alpo-j.sakura.ne.jp/Latest/j_Cylindrical_Maps/j_Cylindrical_Maps.htm.

## References


Acton, Charles H., 1996. Ancillary data services of NASA's navigation and ancillary information facility. Planss 44 (1), 65–70. http://dx.doi.org/10.1016/0032-0633(95)00107-7.

Adriani, Alberto, Filacchione, Gianrico, Di Iorio, Tatiana, Turrini, Diego, Noschese, Raffaella, Cicchetti, Andrea, Grassi, Davide, Mura, Alessandro, Sindoni, Giuseppe, Zambelli, Massimo, Piccioni, Giuseppe, Capria, Maria T, Tosi, Federico, Orosei, Roberto, Dinelli, Bianca M, Moriconi, Maria L, Roncon, Elio, Lunine, Jonathan I, Becker, Heidi N, Bini, Alessadro, Barbis, Alessandra, Calamai, Luciano, Pasqui, Claudio, Nencioni, Stefano, Rossi, Maurizio, Lastri, Marco, Formaro, Roberto, Olivieri, Angelo, 2017. JIRAM, the jovian infrared auroral mapper. Space Sci. Rev. (ISSN: 15729672) 213 (1–4), 393–446. http://dx.doi.org/10.1007/s11214-014-0094-y.

Allison, Michael, 2000. A similarity model for the windy jovian thermocline. Planss 48 (7–8), 753–774. http://dx.doi.org/10.1016/S0032-0633(00)00032-5.

Annex, Andrew, Pearson, Ben, Seignovert, Benoît, Carcich, Brian, Eichhorn, Helge, Mapel, Jesse, von Forstner, Johan, McAuliffe, Jonathan, del Rio, Jorge, Berry, Kristin, Aye, K. Michael, Stefko, Marcel, de Val-Borro, Miguel, Kulumani, Shankar, Murakami, Shin-ya, 2020. SpiceyPy: a pythonic wrapper for the SPICE toolkit. J. Open Source Softw. 5 (46), 2050. http://dx.doi.org/10.21105/joss.02050.

Asay-Davis, Xylar S., Marcus, Philip S., Wong, Michael H., de Pater, Imke, 2011. Changes in Jupiter's zonal velocity between 1979 and 2008. Icarus 211 (2), 1215–1232. http://dx.doi.org/10.1016/j.icarus.2010.11.018.

Atreya, S.K., Wong, M.H., Owen, T.C., Mahaffy, P.R., Niemann, H.B., de Pater, I., Drossart, P., Encrenaz, Th, 1999. A comparison of the atmospheres of Jupiter and saturn: deep atmospheric composition, cloud structure, vertical mixing, and origin. Planss 47 (10–11), 1243–1262. http://dx.doi.org/10.1016/S0032-0633(99)00047-1.

Becker, Heidi N., Alexander, James W., Atreya, Sushil K., Bolton, Scott J., Brennan, Martin J., Brown, Shannon T., Guillaume, Alexandre, Guillot, Tristan, Ingersoll, Andrew P., Levin, Steven M., Lunine, Jonathan I., Aglyamov, Yury S., Steffes, Paul G., 2020. Small lightning flashes from shallow electrical storms on Jupiter. Nature 584 (7819), 55–58. http://dx.doi.org/10.1038/s41586-020-2532-1.

Bluestein, Howard B., Parker, Stephen S., 1993. Modes of isolated, severe convective storm formation along the dryline. Mon. Weather Rev. 121 (5), 1354. http://dx.doi.org/10.1175/1520-0493(1993)121<1354:MOISCS>2.0.CO;2.

Bolton, S.J., Adriani, A., Adumitroaie, V., Allison, M., Anderson, J., Atreya, S., Bloxham, J., Brown, S., Connerney, J.E.P., DeJong, E., Folkner, W., Gautier, D., Grassi, D., Gulkis, S., Guillot, T., Hansen, C., Hubbard, W.B., Iess, L., Ingersoll, A., Janssen, M., Jorgensen, J., Kaspi, Y., Levin, S.M., Li, C., Lunine, J., Miguel, Y., Mura, A., Orton, G., Owen, T., Ravine, M., Smith, E., Steffes, P., Stone, E., Stevenson, D., Thorne, R., Waite, J., Durante, D., Ebert, R.W., Greathouse, T.K., Hue, V., Parisi, M., Szalay, J.R., Wilson, R., 2017. Jupiter's interior and deep atmosphere: The initial pole-to-pole passes with the Juno spacecraft. Science 356 (6340), 821–825. http://dx.doi.org/10.1126/science.aal2108.

Bolton, S.J., Levin, S.M., Guillot, T., Li, C., Kaspi, Y., Orton, G., Wong, M.H., Oyafuso, F., Allison, M., Arballo, J., Atreya, S., Becker, H.N., Bloxham, J., Brown, S.T., Fletcher, L.N., Galanti, E., Gulkis, S., Janssen, M., Ingersoll, A., Lunine, J.L., Misra, S., Steffes, P., Stevenson, D., Waite, J.H., Yadav, R.K., Zhang, Z., 2021. Microwave observations reveal the deep extent and structure of Jupiter's atmospheric vortices. Science 374 (6570), 968–972. http://dx.doi.org/10.1126/science.abf1015.

Brown, S.T., Janssen, M.A., Atreya, S.K., Bolton, S.J., Ingersoll, A.P., Levin, S., Li, C., Lunine, J.I., Orton, G.S., Steffes, P.G., 2018. Cloud morphology associated with jovian lightning. In: AGU Fall Meeting Abstracts, vol. 2018, pp. P33F–3894.

Caplinger, Michael, 2016. Juno Jupiter Junocam 3 RDR L1A V1.0. NASA Planetary Data System, http://dx.doi.org/10.17189/1520279, URL https://pds.nasa.gov/ds-view/pds/viewDataset.jsp?dsid=JUNO-J-JUNOCAM-3-RDR-L1A-V1.0.

Cheng, L., Allison, M., Atreya, S., Brueshaber, S., Fletcher, L.N., Guillot, T., Liming, L., Lunine, J., Miguel, Y., Orton, G., Steffes, P., Waite, J.H., Wong, M.H., Levin, S., Bolton, S., 2024. Super-adiabatic temperature gradient at Jupiter's equatorial zone and implications for the water abundance (in revision). Icarus.

Choi, David S., Showman, Adam P., Vasavada, Ashwin R., Simon-Miller, Amy A., 2013. Meteorology of Jupiter's equatorial hot spots and plumes from cassini. Icarus (ISSN: 0019-1035) 223 (2), 832–843. http://dx.doi.org/10.1016/j.icarus.2013.02.001, URL https://www.sciencedirect.com/science/article/pii/S0019103513000407.

Del Genio, Anthony D., McGrattan, Kevin B., 1990. Moist convection and the vertical structure and water abundance of Jupiter's atmosphere. Icarus (ISSN: 0019-1035) 84 (1), 29–53. http://dx.doi.org/10.1016/0019-1035(90)90156-4, URL https://www.sciencedirect.com/science/article/pii/0019103590901564.

Dowling, T.E., Gierasch, P.J., 1989. Cyclones and moist convection on jovian planets. Bull. Am. Astron. Soc. 21, 946.

Duer, Keren, Gavriel, Nimrod, Galanti, Eli, Kaspi, Yohai, Fletcher, Leigh N., Guillot, Tristan, Bolton, Scott J., Levin, Steven M., Atreya, Sushil K., Grassi, Davide, Ingersoll, Andrew P., Li, Cheng, Li, Liming, Lunine, Jonathan I., Orton, Glenn S., Oyafuso, Fabiano A., Waite, J. Hunter, 2021. Evidence for multiple ferrel-like cells on Jupiter. Geophys. Res. Lett. 48 (23), e95651. http://dx.doi.org/10.1029/2021GL095651.

Fletcher, Leigh N., Kaspi, Yohai, Guillot, Tristan, Showman, Adam P., 2020. How well do we understand the belt/zone circulation of giant planet atmospheres? Space Sci. Rev. 216 (2), 30. http://dx.doi.org/10.1007/s11214-019-0631-9.

Fletcher, L.N., Orton, G.S., Greathouse, T.K., Rogers, J.H., Zhang, Z., Oyafuso, F.A., Eichstädt, G., Melin, H., Li, C., Levin, S.M., Bolton, S., Janssen, M., Mettig, H.-J., Grassi, D., Mura, A., Adriani, A., 2020. Jupiter's equatorial plumes and hot spots: Spectral mapping from gemini/TEXES and Juno/MWR. J. Geophys. Res.: Planets 125 (8), http://dx.doi.org/10.1029/2020JE006399, e2020JE006399, URL https://agupubs.onlinelibrary.wiley.com/doi/abs/10.1029/2020JE006399, e2020JE006399 10.1029/2020JE006399.

Fletcher, Leigh N., Orton, G.S., Rogers, J.H., Giles, R.S., Payne, A.V., Irwin, P.G.J., Vedovato, M., 2017. Moist convection and the 2010–2011 revival of Jupiter's south equatorial belt. Icarus (ISSN: 0019-1035) 286, 94–117. http://dx.doi.org/10.1016/j.icarus.2017.01.001, URL https://www.sciencedirect.com/science/article/pii/S0019103516303839.

Fletcher, L.N., Oyafuso, F.A., Allison, M., Ingersoll, A., Li, L., Kaspi, Y., Galanti, E., Wong, M.H., Orton, G.S., Duer, K., Zhang, Z., Li, C., Guillot, T., Levin, S.M., Bolton, S., 2021. Jupiter's temperate belt/zone contrasts revealed at depth by Juno microwave observations. J. Geophys. Res.: Planets 126 (10), http://dx.doi.org/10.1029/2021JE006858, e2021JE006858, URL https://agupubs.onlinelibrary.wiley.com/doi/abs/10.1029/2021JE006858, e2021JE006858 2021JE006858.

Fountain, J.W., Coffeen, D.L., Doose, L.R., Gehrels, T., Swindell, W., Tomasko, M.G., 1974. Jupiter's clouds: Equatorial plumes and other cloud forms in the pioneer 10 images. Science 184 (4143), 1279–1281. http://dx.doi.org/10.1126/science.184.4143.1279.

Hansen, C.J., Caplinger, M.A., Ingersoll, A., Ravine, M.A., Jensen, E., Bolton, S., Orton, G., 2017. Junocam: Juno's outreach camera. Space Sci. Rev. (ISSN: 15729672) 213 (1–4), 475–506. http://dx.doi.org/10.1007/s11214-014-0079-x.

Holton, James R., 2004. An Introduction to Dynamic Meteorology, Fourth edition In: International Geophysics Series, Academic Press, ISBN: 0-12-354015-1.

Hoskins, B.J., McIntyre, M.E., Robertson, A.W., 1985. On the use and significance of isentropic potential vorticity maps. Q. J. R. Meteorol. Soc. 111 (470), 877–946. http://dx.doi.org/10.1002/qj.49711147002.

Houze, Robert A., 2014. Cloud Dynamics. Academic Press.

Hueso, Ricardo, Sánchez-Lavega, Agustín, Fouchet, Thierry, de Pater, Imke, Antuñano, Arrate, Fletcher, Leigh N., Wong, Michael H., Rodríguez-Ovalle, Pablo, Sromovsky, Lawrence A., Fry, Patrick M., Orton, Glenn S., Guerlet, Sandrine, Irwin, Patrick G.J., Lellouch, Emmanuel, Harkett, Jake, de Kleer, Katherine, Melin, Henrik, Hue, Vincent, Simon, Amy A., Luszcz-Cook, Statia, Sayanagi, Kunio M., 2023. An intense narrow equatorial jet in Jupiter's lower stratosphere observed by JWST. Nat. Astron. 7, 1454–1462. http://dx.doi.org/10.1038/s41550-023-02099-2.

Hueso, Ricardo, Sánchez-Lavega, A., Guillot, T., 2002. A model for large-scale convective storms in Jupiter. J. Geophys. Res. ( Planets) 107 (E10), 5075. http://dx.doi.org/10.1029/2001JE001839.

Imai, Masafumi, Wong, Michael H., Kolmašová, Ivana, Brown, Shannon T., Santolík, Ondřej, Kurth, William S., Hospodarsky, George B., Bolton, Scott J., Levin, Steven M., 2020. High-spatiotemporal resolution observations of Jupiter lightning-induced radio pulses associated with sferics and thunderstorms. Geophys. Res. Lett. 47 (15), e88397. http://dx.doi.org/10.1029/2020GL088397.

Ingersoll, A.P., Gierasch, P.J., Ban, D., Vasavada, A.R., 2000. Moist convection as an energy source for the large-scale motions in Jupiter's atmosphere. Nature 403 (February).

Janssen, M.A., Oswald, J.E., Brown, S.T., Gulkis, S., Levin, S.M., Bolton, S.J., Allison, M.D., Atreya, S.K., Gautier, D., Ingersoll, A.P., Lunine, J.I., Orton, G.S., Owen, T.C., Steffes, P.G., Adumitroaie, V., Bellotti, A., Jewell, L.A., Li, C., Li, L., Misra, S., Oyafuso, F.A., Santos-Costa, D., Sarkissian, E., Williamson, R., Arballo, J.K., Kitiyakara, A., Ulloa-Severino, A., Chen, J.C., Maiwald, F.W., Sahakian, A.S., Pingree, P.J., Lee, K.A., Mazer, A.S., Redick, R., Hodges, R.E.,

Hughes, R.C., Bedrosian, G., Dawson, D.E., Hatch, W.A., Russell, D.S., Chamberlain, N.F., Zawadski, M.S., Khayatian, B., Franklin, B.R., Conley, H.A., Kempenaar, J.G., Loo, M.S., Sunada, E.T., Vorperion, V., Wang, C.C., 2017. MWR: Microwave radiometer for the Juno mission to Jupiter. Space Sci. Rev. 213 (1–4), 139–185. http://dx.doi.org/10.1007/s11214-017-0349-5.

Kurth, W.S., Hospodarsky, G.B., Kirchner, D.L., Mokrzycki, B.T., Averkamp, T.F., Robison, W.T., Piker, C.W., Sampl, M., Zarka, P., 2017. The Juno waves investigation. Space Sci. Rev. 213 (1–4), 347–392. http://dx.doi.org/10.1007/s11214-017-0396-y.

Li, Cheng, Ingersoll, Andrew, Janssen, Michael, Levin, Steven, Bolton, Scott, Adumitroaie, Virgil, Allison, Michael, Arballo, John, Bellotti, Amadeo, Brown, Shannon, Ewald, Shawn, Jewell, Laura, Misra, Sidharth, Orton, Glenn, Oyafuso, Fabiano, Steffes, Paul, Williamson, Ross, 2017. The distribution of ammonia on Jupiter from a preliminary inversion of Juno microwave radiometer data. Geophys. Res. Lett. 44 (11), 5317–5325. http://dx.doi.org/10.1002/2017GL073159, URL https://agupubs.onlinelibrary.wiley.com/doi/abs/10.1002/2017GL073159.

Lin, Yuh-Lang, Joyce, Lara E., 2001. A further study of the mechanisms of cell regeneration, propagation, and development within two-dimensional multicell storms.. J. Atmos. Sci. 58 (20), 2957–2988. http://dx.doi.org/10.1175/1520-0469(2001)058<2957:AFSOTM>2.0.CO;2.

Maddox, Robert A., 1980. Mesoscale convective complexes. Bull. Am. Meteorol. Soc. (ISSN: 00030007, 15200477) 61 (11), 1374–1387, URL http://www.jstor.org/stable/26221473.

Markowski, Paul, Richardson, Yvette, 2010. Mesoscale Meteorology in Midlatitudes. John Wiley and Sons, ISBN: 9780470742136, http://dx.doi.org/10.1002/9780470682104.

NASA, 2023. NASA worldview. URL https://worldview.earthdata.nasa.gov/?v=-108.94411288453438,30.064473216185036,-81.80449460743947,42.39495874554723&t=2020-07-10-T15%3A31%3A22Z. (Accessed on 20 February 2023).

Noschese, R., Huber, L., 2019. Juno JIRAM Bundle. NASA Planetary Data System, http://dx.doi.org/10.17189/1518967, URL https://pds.jpl.nasa.gov/ds-view/pds/viewBundle.jsp?identifier=urn%3Anasa%3Apds%3Ajuno_jiram&version=1.1.

Oyafuso, Fabiano, Levin, Steven, Orton, Glenn, Brown, Shannon T., Adumitroaie, Virgil, Janssen, Michael, Wong, Michael H., Fletcher, Leigh N., Steffes, Paul, Li, Cheng, Gulkis, Samuel, Atreya, Sushil, Misra, Sidharth, Bolton, Scott, 2020. Angular dependence and spatial distribution of Jupiter's centimeter-wave thermal emission from Juno's microwave radiometer. Earth Space Sci. 7 (11), http://dx.doi.org/10.1029/2020EA001254, e2020EA001254, URL https://agupubs.onlinelibrary.wiley.com/doi/abs/10.1029/2020EA001254, e2020EA001254 10.1029/2020EA001254.

Porco, C.C., West, R.A., McEwen, A., Del Genio, A.D., Ingersol, A.P., Thomas, P., Squyres, S., Dones, L., Murray, C.D., Johnson, T.V., Burns, J.A., Brahic, A., Neukum, G., Veverka, G., Barbara, J.M., Denk, T., Evans, M., Ferrier, J.J., Geissler, P., Helfenstein, P., Roatsch, T., Throop, H., Tiscareno, M., Vasavadal, A.R., 2003. Cassini imaging of Jupiter's atmosphere, satellites, and rings. Science 299, 1541–1547. http://dx.doi.org/10.1126/science.1079462.

Rayner, J.T., Toomey, D.W., Onaka, P.M., Denault, A.J., Stahlberger, W.E., Vacca, W.D., Cushing, M.C., Wang, S., 2003. SpeX: A medium-resolution 0.8-5.5 micron spectrograph and imager for the NASA infrared telescope facility. Publ. Astron. Soc. Pac. 115 (805), 362–382. http://dx.doi.org/10.1086/367745.

Rogers, J.H., 2019a. Jupiter's north equatorial belt & jet I. Cyclic expansions & planetary waves. J. Br. Astron. Assoc. URL https://britastro.org/journal_contents_ite/jupiters-north-equatorial-belt-jet-i-cyclic-expansions-planetary-waves. (Accessed on 1 February 2024).

Rogers, John H., 2019b. Jupiter's north equatorial belt & jet: II. Acceleration of the jet & the NEB fade in 2011-'12. J. Br. Astron. Assoc. 129, 95–102. http://dx.doi.org/10.48550/arXiv.1809.09719.

Rogers, J.H., 2021a. Jupiter in 2021, Report no.1: View at the start of the apparition. J. Br. Astron. Assoc. URL https://britastro.org/section_information_/jupiter-section-overview/jupiter-in-2021-22/jupiter-in-2021-report-no-1-view-at-the-start-of-the-apparition. (Accessed on 10 March 2023).

Rogers, J.H., 2021b. Jupiter in 2021, Report no.2. J. Br. Astron. Assoc. URL https://britastro.org/section_information_/jupiter-section-overview/jupiter-in-2021-22/jupiter-in-2021-report-no-2. (Accessed on 10 March 2023).

Rogers, J.H., 2021c. Jupiter in 2021, Report no.6: Bright plume outbreaks in the narrow NEB(S). J. Br. Astron. Assoc. URL https://britastro.org/section_information_/jupiter-section-overview/jupiter-in-2021-22/jupiter-in-2021-report-no-6-bright-plume-outbreaks-in-the-narrow-nebs. (Accessed on 10 March 2023).

Rogers, J.H., 2022. Jupiter in 2021/22, report no.7: Equatorial region update. J. Br. Astron. Assoc. URL https://britastro.org/section_information_/jupiter-section-overview/jupiter-in-2021-22/jupiter-in-2021-22-report-no-7-equatorial-region-update. (Accessed on 1 February 2024).

Rogers, J.H., Adamoli, G., 2019c. Jupiter's north equatorial belt & jet Part III: The 'great northern upheaval' in 2012. J. Br. Astron. Assoc. 129, 158–169. http://dx.doi.org/10.48550/arXiv.1809.09736.

Rogers, John, Mizumoto, Shinji, 2022. Jupiter in 2022/23: Report no.2. Br. Astron. Assoc. URL https://britastro.org/section_information_/jupiter--section--overview/jupiter--in--2022--23/jupiter--in--2022--23--report--no--2.

Rogers, John H., Mizumoto, Shinji, Hansen, Candice, Eichstädt, Gerald, Orton, Glenn, Momary, Thomas, Adamoli, Gianluigi, Bullen, Robert, Jacquesson, Michel, Mettig, Hans-Jörg, 2022. The transformation of Jupiter's north equatorial belt in 2021-22. In: European Planetary Science Congress. pp. EPSC2022–17. http://dx.doi.org/10.5194/epsc2022-17.

Sankar, R., Wong, M.H., Palotai, C., Brueshaber, S., 2024. Role of eddy vapor transport in driving water convection on Jupiter. Icarus submitted for publication.

Schumacher, Russ S., Rasmussen, Kristen L., 2020. The formation, character and changing nature of mesoscale convective systems. Nat. Rev. Earth Environ. 1 (6), 300–314. http://dx.doi.org/10.1038/s43017-020-0057-7.

Stoker, C.R., 1986. Moist convection: A mechanism for producing the vertical structure of the jovian equatorial plumes. Icarus 67 (1), 106–125. http://dx.doi.org/10.1016/0019-1035(86)90179-X.

Stoker, C.R., Hord, C., 1985. Vertical cloud structure of Jupiter's equitorial plumes. Icarus 64 (3), 557–575. http://dx.doi.org/10.1016/0019-1035(85)90076-4.

Sugiyama, K., Nakajima, K., Odaka, M., Ishiwatari, M., Kuramoto, K., Morikawa, Y., Nishizawa, S., Takahashi, Y.O., Hayashi, Y.-Y., 2011. Intermittent cumulonimbus activity breaking the three-layer cloud structure of Jupiter. Geophys. Res. Lett. 38 (13), http://dx.doi.org/10.1029/2011GL047878, URL https://agupubs.onlinelibrary.wiley.com/doi/abs/10.1029/2011GL047878.

Sugiyama, K., Nakajima, K., Odaka, M., Kuramoto, K., Hayashi, Y.Y., 2014. Numerical simulations of Jupiter's moist convection layer: Structure and dynamics in statistically steady states. Icarus (ISSN: 00191035) 229, 71–91. http://dx.doi.org/10.1016/j.icarus.2013.10.016.

Thomson, Stephen I., McIntyre, Michael E., 2016. Jupiter's unearthly jets: A new turbulent model exhibiting statistical steadiness without large-scale dissipation*. J. Atmos. Sci. 73 (3), 1119–1141. http://dx.doi.org/10.1175/JAS-D-14-0370.1.

Tollefson, Joshua, Wong, Michael H., Pater, Imke de, Simon, Amy A., Orton, Glenn S., Rogers, John H., Atreya, Sushil K., Cosentino, Richard G., Januszewski, William, Morales-Juberías, Raúl, Marcus, Philip S., 2017. Changes in Jupiter's zonal wind profile preceding and during the Juno mission. Icarus 296, 163–178. http://dx.doi.org/10.1016/j.icarus.2017.06.007.

USGS-Astrogeology, USGS-astrogeology/ISIS3: ISIS 8.0.0 public release, URL https://github.com/DOI-USGS/ISIS3/releases.

Vallis, Geoffrey K., 1996. Potential vorticity inversion and balanced equations of motion for rotating and stratified flows. Q. J. R. Meteorol. Soc. 122 (529), 291–322. http://dx.doi.org/10.1002/qj.49712252912.

Vasavada, Ashwin R., Ingersoll, Andrew P., Banfield, Don, Bell, Maureen, Gierasch, Peter J., Belton, Michael J.S., Orton, Glenn S., Klaasen, Kenneth P., DeJong, Eric, Breneman, H. Herbert, Jones, Todd J., Kaufman, James M., Magee, Kari P., Senske, David A., 1998. Galileo imaging of Jupiter's atmosphere: The great red spot, equatorial region, and white ovals. Icarus 135 (1), 265–275. http://dx.doi.org/10.1006/icar.1998.5984.

Vizy, Edward K., Cook, Kerry H., 2018. Mesoscale convective systems and nocturnal rainfall over the west african sahel: role of the inter-tropical front. Clim. Dyn. 50 (1–2), 587–614. http://dx.doi.org/10.1007/s00382-017-3628-7.

Wong, Michael H., Bjoraker, Gordon L., Goullaud, Charles, Stephens, Andrew W., Luszcz-Cook, Statia H., Atreya, Sushil K., de Pater, Imke, Brown, Shannon T., 2023. Deep clouds on Jupiter. Remote. Sens. (ISSN: 2072-4292) 15 (3), http://dx.doi.org/10.3390/rs15030702, URL https://www.mdpi.com/2072-4292/15/3/702.

Wong, Michael H., Mahaffy, Paul R., Atreya, Sushil K., Niemann, Hasso B., Owen, Tobias C., 2004. Updated galileo probe mass spectrometer measurements of carbon, oxygen, nitrogen, and sulfur on Jupiter. Icarus 171 (1), 153–170. http://dx.doi.org/10.1016/j.icarus.2004.04.010.

Wong, M.H., Oyafuso, F.A., Imai, M., Kolmasova, I., Mizumoto, S., Levin, S.M., Sankar, R., Simon, A.A., Brueshabern, S., Orton, G.S., Atreya, S.K., Li, C., Bolton, S.J., 2024. Radio pulse power distribution of lightning in Jupiter's 2021–2022 stealth superstorms.. AGU Adv. submitted for publication.

Zhang, Zhimeng, Adumitroaie, Virgil, Allison, Michael, Arballo, John, Atreya, Sushil, Bjoraker, Gordon, Bolton, Scott, Brown, Shannon, Fletcher, Leigh N., Guillot, Tristan, Gulkis, Samuel, Hodges, Amoree, Ingersoll, Andrew, Janssen, Michael, Levin, Steven, Li, Cheng, Li, Liming, Lunine, Jonathan, Misra, Sidharth, Orton, Glenn, Oyafuso, Fabiano, Steffes, Paul, Wong, Michael H., 2020. Residual study: Testing Jupiter atmosphere models against Juno MWR observations. Earth Space Sci. 7 (9), http://dx.doi.org/10.1029/2020EA001229, e2020EA001229, URL https://agupubs.onlinelibrary.wiley.com/doi/abs/10.1029/2020EA001229, e2020EA001229 2020EA001229.